REPORT DOCUMENTATION PAGE

Form Approved
OMB No. 0704-0188

1. AGENCY USE ONLY (Leave blank)	2. REPORT DATE	3. REPORT TYPE AND DATES COVERED
		FINAL

4. TITLE AND SUBTITLE
Photon-Counting Spatial Light Modulator Technology
Development

5. FUNDING NUMBERS
61102F
8691/02

6. AUTHOR(S)
Dr Richard B. Holmes

7. PERFORMING ORGANIZATION NAME(S) AND ADDRESS(ES)

Rockwell International Corporation

8. PERFORMING ORGANIZATION REPORT NUMBER

9. SPONSORING / MONITORING AGENCY NAME(S) AND ADDRESS(ES)
AFOSR/NE
110 Duncan Avenue Suite B115
Bolling AFB DC   20332-0001

DTIC
SELECTED
MAR 2 7 1995
G

10. SPONSORING / MONITORING AGENCY REPORT NUMBER

F49620-92-C-0064

11. SUPPLEMENTARY NOTES

12a. DISTRIBUTION / AVAILABILITY STATEMENT

APPROVED FOR PUBLIC RELEASE: DISTRIBUTION UNLIMITED

12b. DISTRIBUTION CODE

13. ABSTRACT (Maximum 200 words)

SEE FINAL REPORT ABSTRACT

19950323 144

14. SUBJECT TERMS			15. NUMBER OF PAGES
			16. PRICE CODE

17. SECURITY CLASSIFICATION OF REPORT	18. SECURITY CLASSIFICATION OF THIS PAGE	19. SECURITY CLASSIFICATION OF ABSTRACT	20. LIMITATION OF ABSTRACT
UNCLASSIFIED	UNCLASSIFIED	UNCLASSIFIED	UNCLASSIFIED

Standard Form 298 (Rev. 2-89)

ROCKWELL INTERNATIONAL CORPORATION
ROCKETDYNE DIVISION
F49620-92-C-0064--DEF
Program Code 2D10

PHOTON-COUNTING SPATIAL LIGHT MODULATOR TECHNOLOGY DEVELOPMENT
Final Technical Report
September 1992 - September 1994
30 October 1994   **AFOSR-TR- 95 0149**

Effective Date Of Contract: 01 September 1992
Contract Expiration Date: 30 November 1994
Amount Of Contract Dollars: $349,240

PRINCIPAL INVESTIGATOR: RICHARD B. HOLMES 818/586-3030

PREPARED BY

DR. JEFFREY H. HUNT
MEMBER TECHNICAL STAFF

APPROVED BY

ROBERT N. HINDY
PROGRAM MANAGER
ADVANCED TECHNOLOGY
818/586-0443

Accesion For		
NTIS CRA&I		☒
DTIC TAB		☐
Unannounced		☐
Justification		
By		
Distribution /		
Availability Codes		
Dist	Avail and / or Special	
A-1		

The views and conclusions contained in this document are those of the authors and should not be interpreted as necessarily representing the official policies or endorsements, either expressed or implied, of the Defense Advanced Research Projects Agency or the U. S. Government.

Sponsored by
Defense Advanced Research Projects Agency
DARPA Order No. 8691
Monitored by AFOSR under Contract No. F49620-92-C-0064

CONTENTS

CONTENTS

FIGURES

TABLES

1.0 ABSTRACT

The goal of this program is to measure and improve the performance of photon-counting spatial light modulators operating in an optically-addressed reflection mode. Experimental results are obtained for silicon devices. These device consists of an avalanche photodiode (APD) operated in the Geiger mode with the front and back surface of the diode forming an asymmetric Fabry-Perot cavity. The phase delay within the cavity is modified directly by the avalanche via the free-carrier refractive index or by Joule heating. Experiments were conducted first with the write laser beam at 1064 nm and the read beam at the same wavelength and second with the write beam at 850 nm and the read beam at 1300 nm. The device differs qualitatively from other approaches such as smart pixels by virtue of its photon-counting sensitivity, its low cost and its ability to form a spatially-coherent read-out wavefront.

Contrast modulation of up to 98% (2:1) was observed at photon-counting light levels relative to the off state, with 50 nanosecond delays between the read and write beam and 6 nanoJoules of electrical energy per bit. This result is ascribed to Joule heating. Faster response was also achieved at the expense of reduced contrast modulation; 8% modulation was observed with 3 nsec pulses, 0 nsec write-read delay and 4.3 nJ/bit. The observed radius of the optical modulation was 3 microns. Optical gains of 8.5×10^5 were observed; camera saturation precluded measurement of higher gains. The lasers operated at a maximum of 20 kHz, which limited the frame rate used in the experiment. Frame rates of 1 MHz or more are expected with this technology, based on published frame rates for APDs. The corresponding throughput of the device is 2.5 Terabits/sec/cm^2.

It is believed that 1 GHz frame rates will be the limit for properly designed single-pixel silicon devices, requiring approximately 1.2 nanoJoules of electrical energy per bit. The expected radius of contrast modulation will be about 2 microns. The operating voltage will be reduced from approximately 250 volts to approximately 45 volts. These advances will be achieved by using an epitaxially-grown shallow-junction device structure and free-carrier refractive index modulation. These advances should be achieved with a reduction in contrast modulation to 40% and a reduction in optical gain to about 10^4. The throughput for such devices will be limited by thermal runaway, which will limit frame rates to about 80 MHz for array structures. The primary limit on noise will be set by thermal avalanching and parasitic avalanches and is crudely estimated to yield a bit error rate of about 9×10^{-10} at -25 °C. Uniform deposition of current will be maintained by using a transparent Cr/Au screen electrode on the front surface and will allow electrical addressing as well as optical addressing. The use of epitaxial fabrication will ensure optical-quality devices with an

expected cost per pixel of about 0.01 cents, based on quotes from manufacturers for the shallow junction device. The shallow-junction device is expected to require temperature deviations of less than ± 2 C for proper operation, though a larger temperature range may be acceptable for certain applications.

Several potential applications are identified as follows: a low-light level laser radar receiver, an optically-controlled passive-matrix display, a large-area optical switch and an optically-addressed parallel optical transistor, an all-optical serial-to-parallel converter and a fast beam-steering device.

2.0 INTRODUCTION

When light impinges on an avalanche photodiode (APD) with voltage applied, a localized avalanche of charge carriers results as shown in Figure 1. The basic electrical properties of the avalanche are well known, whether the diode operates in conventional linear mode,[1,2] or in the less common Geiger mode.[3,4] However, the spatial and temporal details of breakdown have remained unknown until recently. For spatial light modulation to occur, the breakdown filament must be spatially localized for the time constant of the optical phenomena that causes modulation.[5] In this effort, this basic issue was resolved in the affirmative, for a range of external voltages and resistances. The experiment presented herein forms actual images of the avalanche current and heating caused by it. The results are temporally resolved by pulsing both the excitation and probe light and introducing a delay between the two. Based on these results, an optically-addressed spatial light modulator has been designed and tested which has photon-counting sensitivity, frame rates of up to 30 MHz and a resolution of 3 microns at the face of the device.

There are several optical mechanisms which may be present in a silicon APD when a voltage is applied and current flows.[6,7,8,9,10] Of these, the strongest is the thermo-optic effect.[6,9] The thermo-optic effect arises because electrical breakdown causes localized Joule heating which in turn modifies the refractive index of a silicon avalanche photodiode as indicated in Figure 2. The refractive index modulation can be read out most easily by photons whose energy is less that the band-gap energy of the material. In our experiments, the read-out is performed in reflection with light at 1300 nm, using the APD's natural Fabry-Perot geometry. The excitation of the avalanche photodiode (APD) is controlled using focused, short-pulse, 850 nm light. Spatial resolution of the heating profile is accomplished using a digital camera that integrates the intensity of the 1300 nm probe over many excitation cycles of the APD. Temporal resolution is performed by delaying the 1300 nm probe pulse with respect to the excitation pulse at 850 nm. Both the response strength and spatial profile are measured as a function of overvoltage and delay, as described in Section 4.

To understand how the measured results scale, a theory of avalanche-induced light modulation is needed. The theory presented in Section 3 emphasizes the thermo-optic effect, but the free-carrier effect is also included, since it was observed. Important assumptions are also discussed and justified and the theory is compared to the experimental results in Section 5. Results presented herein for both the thermo-optic effect and the free-carrier effect have been recently been confirmed.[9,10]
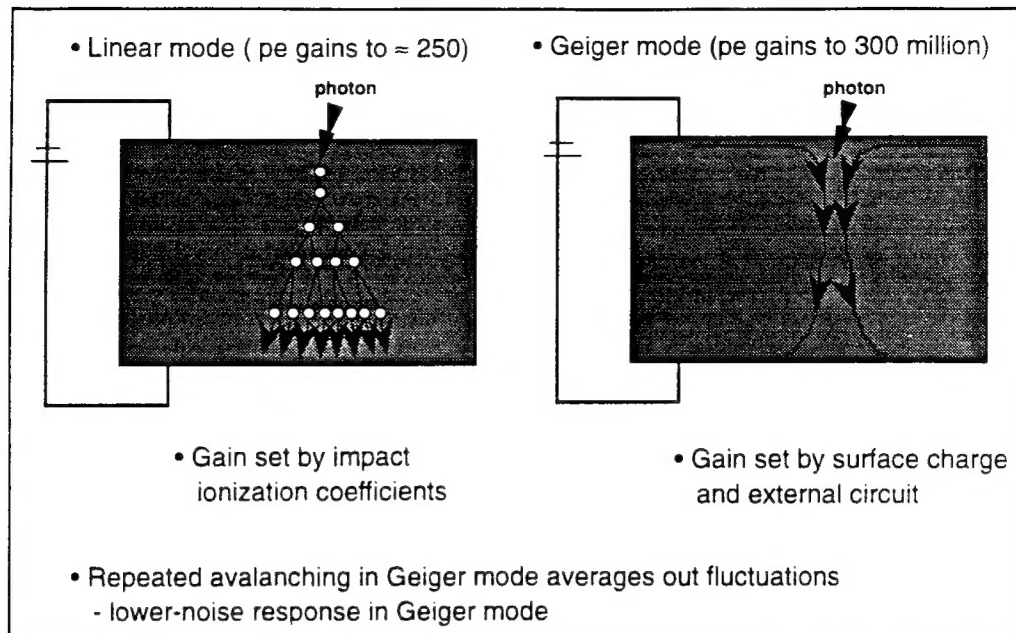
Figure 1. Modes of operation of an avalanche photodiode.
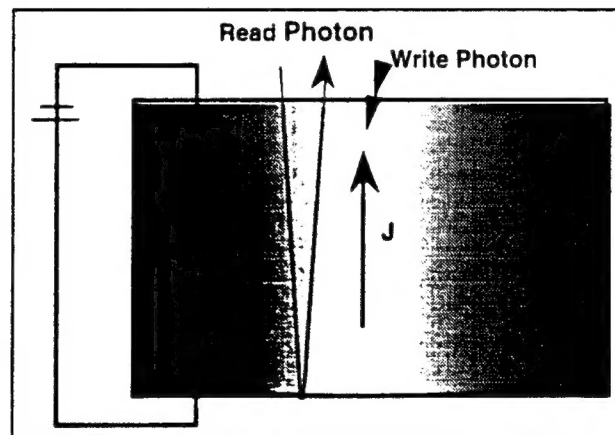
*Figure 2. Light modulation with the thermo-optic effect
in avalanche photodiodes.*

With a thorough development of the theory and practice of spatial light modulation in avalanche photodiodes, the next step is to determine potential applications for the device. Potential applications of the approach are discussed in the Sections 6 and 7, with an emphasis on a low-cost spatial light modulator (SLM). An understanding of the basic physics allows scaling of the sensitivity, speed, resolution and noise of the lab results. An appreciation of the manufacturing processes allows a specification of a device that is inexpensive and reliable. Finally, a detailed knowledge of the potential applications ensure that a useful device will be the result.

3.0 THEORY

The thermo-optic effect in an APD is a four-step process which is summarized in Figure 2. First, a photon is absorbed with a quantum efficiency η that depend on the device material, thickness and doping. The absorption process will then initiate an avalanche with a probability that depends on both the photon wavelength and the applied voltage. A localized avalanche proceeds which causes localized heating. Finally, the induced heating causes expansion of the diode material and alteration of its electronic properties; these effect a change in refractive index. This refractive index variation can be read out directly using light of the same or different wavelength. The refractive index modulation is conveniently read-out using contrast modulation, since the diode naturally forms a Fabry-Perot cavity, i.e., a Fizeau interferometer. These steps are described in more detail in the following subsections, starting with an optical analysis that may be more familiar to most readers.

3.1 OPTICAL CHARACTERIZATION

The reflectivity of a Fabry-Perot cavity depends on the refractive index through the round-trip phase ϕ and this reflectivity is given by

$$M = | R_f - \exp(i\phi)R_b |^2 / |1 - \exp(i\phi)R_fR_b |^2 \qquad (1)$$

where R_f is the front-surface amplitude reflectivity, corresponding to an air-silicon interface or an anti-reflection-coated interface. The rear-surface amplitude reflectivity, R_b, corresponds to a metal-silicon interface. The rear-surface amplitude reflection coefficient is approximately 0.5 and for the front surface from 0.3 to 0.2,[11] for the APD used.[12] The round-trip phase delay ϕ depends on the material, temperature and thickness of the device and can be determined for the purposes of this experiment from a measurement of the overall device reflectivity M with the voltage off; multiple measurements at different wavelengths can also determine the optical parameters of the device.

Absorptive and diffractive losses as light traverses the diode should also be included in Eq.(1). The absorptive loss for the read-out light ranges from a few percent at 1064 nm down to less than 10^{-6} percent at 1300 nm. The diffractive loss may be computed to first order from Eqs. (2)-(3) below and can be substantial.

The phase change $\delta\phi$ experienced by a read-out beam may be obtained, as well as the first-order change in log-amplitude, $A(z)/A_0$, arising from this phase change, using well-known formulae:[13,14]

$$\delta\phi(x,z=2\Delta z) = k_0\cos\theta \int \delta n \, dz \qquad (2)$$

$$A(z)/A_0 = \exp\left((1/2 \, k_0 \, n_0) \int [\nabla^2 \delta\phi(x=0,z)] \, dz/\cos\theta \right) \qquad (3)$$

where k_0 is the optical wavenumber, equal to $2\pi/\lambda$; λ is the free-space optical wavelength; δn is the refractive index perturbation; n_0 is the refractive index of the diode material, roughly equal to 3.5 for silicon in the infrared; and $\cos\theta$ is the angle of propagation in the crystal relative to the diode surface normal. The integrals are over twice the depth of the diode; the diode depth Δz is about 35 microns for the diode used.[11] Note that absorptive losses are not included; no substantial absorption is expected from the electrical avalanche.[8] From Eqs.(2)-(3) the round-trip phase delay and the diffractive loss may be obtained:

$$\phi = k_0 \, \cos\theta \int \delta n \, dz + \phi_0 \qquad (4)$$

$$A(x,2\Delta z)/A_0 = \exp\left(- \delta\phi(x=0,z=2\Delta z) \, \Delta z / (\cos\theta \, k_0 n_0 \, r_{opt}2) \right) \qquad (5)$$

where ϕ_0 is the phase retardation when the diode is not excited and the (measured) half-width at half-max of the optical spot is r_{opt} Eq.(5) assumes uniform heating over the diode depth and a parabolic transverse heating profile.

Perturbations in this round-trip phase are caused by heating and the free-carrier refractive index; heating profiles are derived from the well-known thermal diffusion equation treated in the following paragraphs. It will be seen that phase changes of 0.5 radians and contrast modulation of 90% is obtainable with about 6 degrees of heating.

3.2 THERMAL CHARACTERIZATION

It is anticipated that the refractive index is primarily modulated by the induced temperature changes; Modulation to a lesser extent may also result from the material density and the density of carriers. Hence for small perturbations in the refractive index,

$$\delta n = + (\partial n/\partial T) \, \delta T + (\partial n/\partial\rho) \, \delta\rho + (\partial n/\partial\rho_e) \, \delta\rho_e + (\partial n/\partial\rho_h) \, \delta\rho_h \qquad (6)$$

where $\partial n/\partial T = 1.9 \times 10^{-4}\,K^{-1}$,[15] δT is the induced temperature change, $\delta\rho$ is the induced change in material density and $\delta\rho_{e,h}$ is the density of electrons and holes, respectively. The induced density change is ignored in this section because the localized heating causes local stresses in the solid that are relieved acoustically, so that the crystal achieves structural equilibrium within a few nanoseconds and the resulting state of deformation gives a refractive index proportional to temperature. The free-carrier densities changes can be large if the diode is biased appropriately: the refractive index coefficient for electrons is $\partial n/\partial\rho_e = -8.5 \times 10^{-22}\,cm^3$ and the coefficient for holes is about $-5.0 \times 10^{-22}\,cm^3$. Thus, free-carrier effects become comparable to temperature effects with carrier densities of the order of $4 \times 10^{17}\,cm^{-3}$; this can be achieved with breakdown currents of about 25 mA, if the breakdown filament remains localized to a few microns. However, operation at such high current levels is not needed for observation of the thermal effect and so the result is that the refractive index is proportional to temperature.

The basic thermal response is given by the following equation:

$$[c_p\,\partial/\partial t - \kappa\nabla^2\,]\,\delta T = \mathbf{j}\cdot\mathbf{E} \qquad (7)$$

where c_p is the specific heat ($1.65\,J/(cm^3K)$ for silicon) t is time, κ is the thermal conductivity (equal to $1.48\,W/(cmK)$ for silicon), δT is the temperature variation in degrees Kelvin, j is the local current density and $\mathbf{E}$ is the local electric field.

The discussion of the following section specifies the spatial and temporal distribution of the source of the photo-induced diode heating. From those analyses, it is found that the source term $\mathbf{j}\cdot\mathbf{E}$ is approximately $I_{ss}V_{ss}/\pi r^2\Delta z$, the Joule heat per unit volume. Here r is the radius of the discharge, Δz is the thickness of the device and steady-state current conditions apply with current I_{ss} and diode voltage V_{ss}.

An additional prerequisite for solution of Eq.(7) is the specification of the boundary conditions. This requires specification of the heat fluxes through the surface of the silicon diode. The fluxes through the front and back surfaces might be important and such fluxes reduce the temperature caused by heating. For the conditions of the experiment, it is shown that these fluxes are not significant and this is justified below on both experimental and theoretical grounds.

Based on the these remarks, a simple but adequate model for avalanche diode heating assumes that an electrical avalanche provides a line source of heat and that the front and back surfaces are

insulative for the time scales relevant to the experiment. A Fourier transform analysis then yields the following expression for the temperature distribution as a function of time t and radius r = |x| from the excitation.

$$T(r,t) = \frac{1}{4\pi^2} \int \int \exp(i\mathbf{k} \cdot \mathbf{x})(- (\kappa/c_p) k^2(t-t')) (\mathbf{E} \cdot \mathbf{j}(k,t') /c_p) \, dt' \, dk^2 \tag{8}$$

$$\approx \frac{I_{ss}V_{ss}}{2\pi\Delta z\kappa} \int (1-\exp(- (\kappa/c_p) k^2 t) \frac{J_0(kr)}{k} \, dk. \tag{9}$$

The last equation is integrated numerically to give the results shown in Figures 3 and 4. The parameters are chosen for their relevance to the experiment and may be scaled using Eq.(9). Figure 3 shows the strength and spatial extent of the temperature response when the leading factor, $I_{ss}V_{ss}/(2\pi\Delta z\kappa)$, is equal to 6.03 degrees Kelvin, for read/write delays of 50 and 100 nanoseconds. This value for the leading factor is consistent with expected electrical conditions, as discussed in the next section. The plot is truncated at radii less than 0.5 microns, where the assumed line source gives physically unrealistic results. The predicted average phase change in the central 2.0 micron region is about 5 degrees and the observed radius of the temperature perturbation is predicted to be about 1.7 and 2.0 microns for the 50 and 100 nanosecond delay, respectively.

Predicted Thermal Response vs Radius
(285 V, 35 micron thickness, insulative front and back, line source)
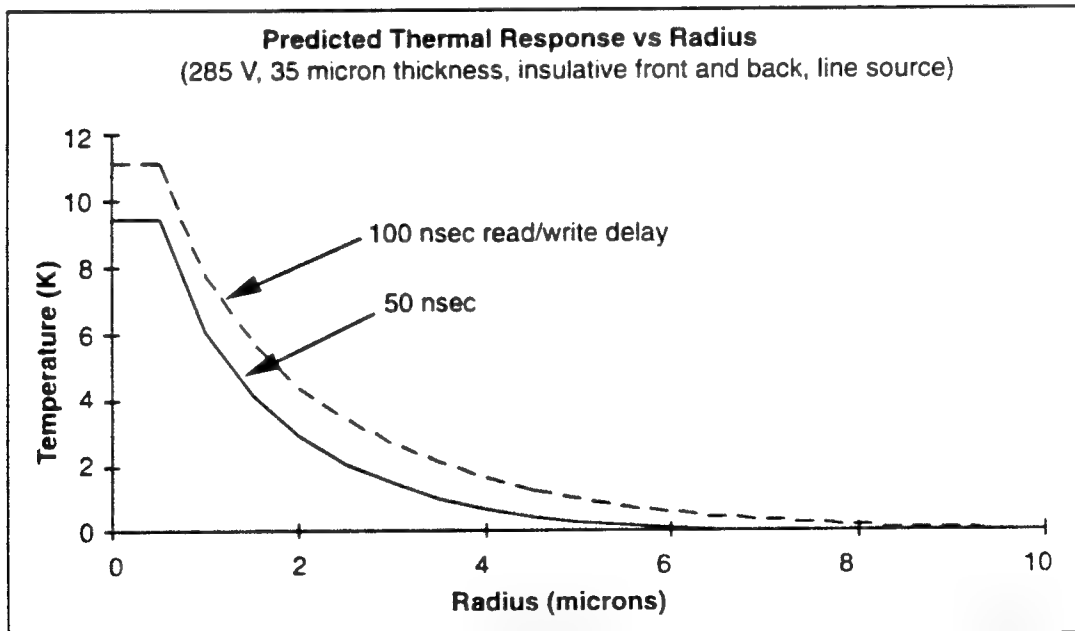
Figure 3. Predicted thermal response versus radius. The read/write delays are 50 nsec (solid line) and 100 nsec (dashed line). The overvoltage is 40 V, the circuit resistance is 50 kΩ and the silicon diode thickness is 35 microns.

Predicted Thermal Response vs Time
(285 V, 35 micron thickness, insulative front and back, line source)
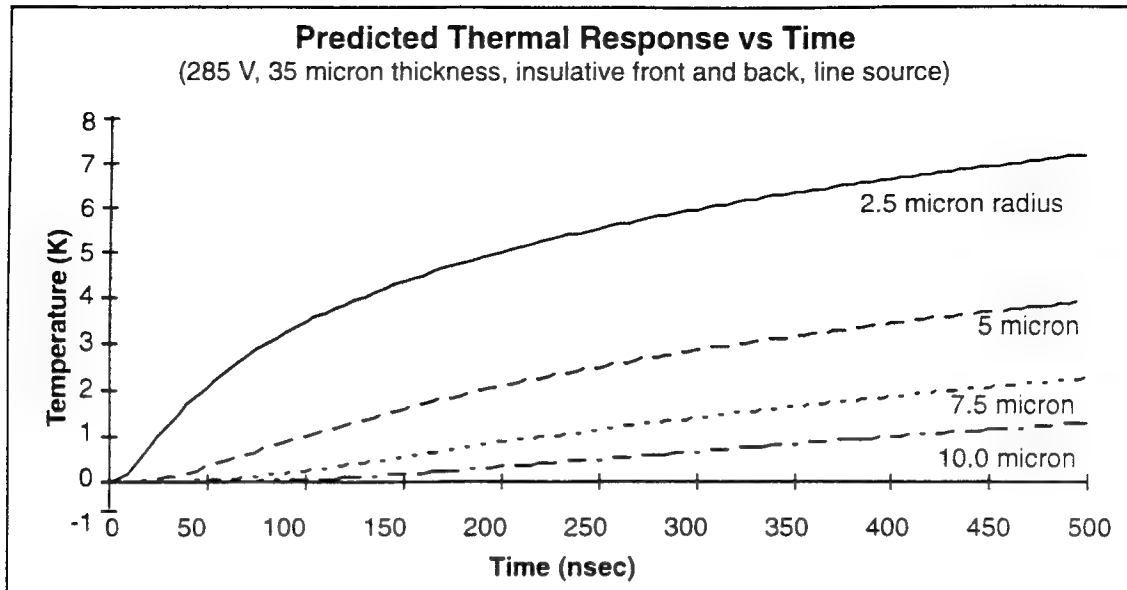
Figure 4. Predicted thermal response versus read/write delay. The transverse radial separations from the source are 2.5 (solid line), 5.0 (dashed), 7.5 (dotted) and 10.0 microns (dot-dashed). The relevant parameters are as in Figure 4.

This result justifies the approximation that the front and back surfaces may be treated as insulative. The figure shows that heat only diffuses at most 4 microns for excitations of duration less than 100 nanoseconds. Since the device thickness of 35 microns is much thicker than this 4 microns, only a small fraction of the heat along the line source can diffuse through the silicon to the front or back surfaces. Thus even if these surfaces are highly conductive and at ambient temperature, they will not transfer enough heat to substantially alter the overall thermal response.

Figure 4 graphs the predicted temperature versus time for several radii from the line source. The temperature rise is seen to be linear at early times and the temperature rise slowly saturates with time. The saturation is quickest for the smallest separations, especially below about 5 microns. This saturation of the thermal response implies that there is only limited value in increasing the duration of the electrical excitation.

To obtain some simpler analytic results, one observes that there are two basic thermal regimes, transient and steady-state. The transient regime applies when the deposited heat has insufficient time to diffuse. In such instances, the heat is more concentrated and the thermo-optic effect is strongest, given a fixed quantity of deposited heat. The second regime is the steady-state regime, in which the heat is allowed time to diffuse and in which more time is available to read out the excitation. The transient regime applies for radii satisfying

$$r > \sqrt{\kappa t / c_p} \qquad (10)$$

Given that Eq. (10) applies, the thermo-optic phase change is given by ignoring the second term on the left-hand side of Eq. (7) and integrating over time and then integrating the implied refractive index over the diode depth z. This gives a phase change $\delta\phi(r,t)$ expressed by Eq. (11) below. The alternative quasi-steady-state result is obtained by ignoring the time derivative in Eq. (7), applying Gauss' Law to a cylindrical volume and integrating. This result is given in Eqs. (12)-(13):

$$\delta\phi = 2k_0 \, \Delta z \, \cos\theta \, (\partial n/\partial T) \, \{ S \, [\, 2\kappa t \, /r_0^2 c_p \,] \}, \qquad \text{for } \kappa t/c_p r_0^2 < 1, \, r<r_0. \quad (11)$$

$$\delta\phi = 2k_0 \, \Delta z \, \cos\theta \, (\partial n/\partial T) \, \{ T_0(t) - (1/2)S \, (r/r_0)^2 \}, \qquad \text{for } \kappa t/c_p r_0^2 \gg 1, \, r<r_0. \quad (12)$$

$$\delta\phi = 2k_0 \, \Delta z \cos\theta \, (\partial n/\partial T) \, \{ T_0(t) - S[\, 1/2 + \ln(r/r_0)] \}, \quad \text{for } \kappa t/c_p r_0^2 \gg 1, \, r>r_0. \quad (13)$$

In these expressions $S = GeV_{ss}/(2\pi \, t \, \kappa \, \Delta z)$, $G = (1/e)\int I_{ss}dt$ is the photoelectron gain, e is electric charge and t and r are the duration and radius of the thermal response, respectively. $T_0(t)$ is the induced temperature change at the center of the electrical excitation, which depends on time and ro is the radius of the electrical discharge. This temperature change $T_0(t)$ can be expressed fairly accurately in terms of the radius r_z at which the temperature expression drops to zero:

$$T_0(t) = S[\, 1/2 + \ln(r_z/r_0) \,] \qquad (14)$$

In the analysis of the experimental data, r_z is measured and is the half-width at full maximum of the contrast modulation.

3.3 ELECTRICAL CHARACTERIZATION

To complete a physical specification of the problem, the current density and the electrical field must be defined. The electric field is simply related to the device voltage and current. The basic behavior of these latter quantities is well-known and summarized in Figure 5.[3]
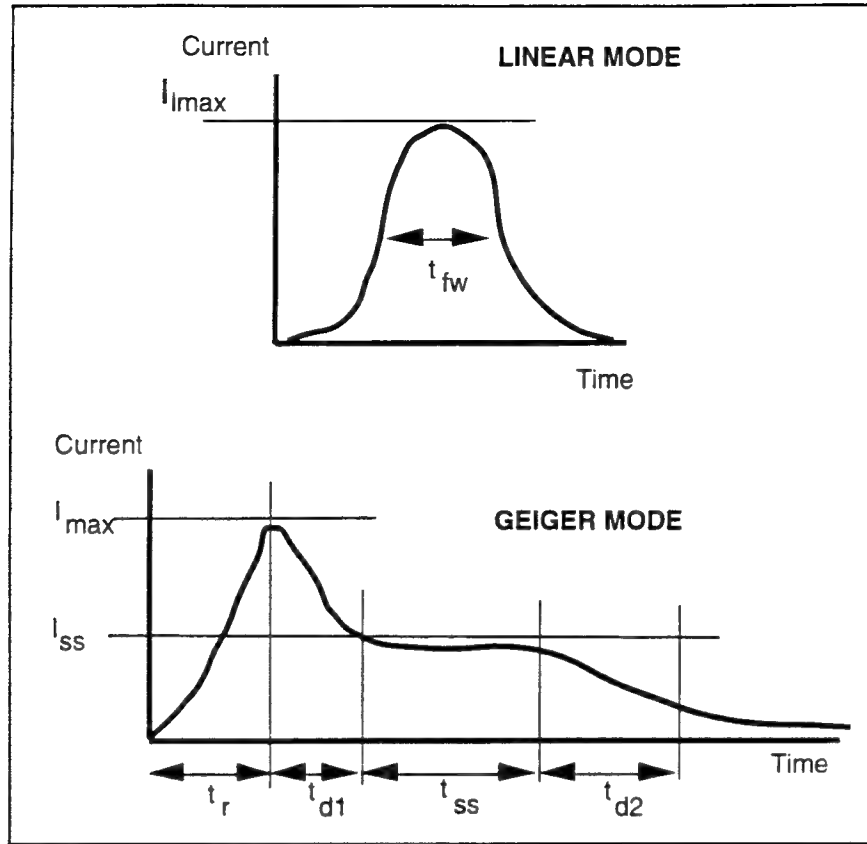
Figure 5. Electrical pulse profiles of the avalanche photodiode.

In Figure 5 the relevant quantities are the full-width at half max of the pulse in the linear mode, t_{fw}; the rise time of the electrical response of the diode, t_r; the decay time for discharge of the surface charge on the diode, t_{d1}; the duration of the steady-state current, t_{ss}; and he final decay time of the steady-state current, t_{d2}. These quantities, as well as the currents I_{max} and I_{ss} and the diode voltages V_{max} and V_{ss}, can be expressed in terms of the electrical properties of the diode and circuit. These properties may be expressed in terms of the capacitance of the diode, C; the load resistance in the circuit, R_L, which is chosen to optimize optical response; the diode resistance, R_D; the circuit voltage, V; and the diode's breakdown voltage, V_B. According to the Haitz model for Geiger mode operation, the relevant expressions are as follows, applicable in the case of passive quenching of the device:

$$t_r = 0.5 \, t_{fw} \tag{16}$$

$$t_{d1} = CR_L R_D / (R_L + R_D) \tag{17}$$

$$< t_{ss} > = t_o \exp(I_{ss}/I_o); \, t_o, I_o \text{ set by the device} \tag{18}$$

$$t_{d2} = CR_L \tag{19}$$

$$I_{max} = (V - V_B) / R_D \tag{20}$$

RI/RD95-106

11

$$I_{ss} = (V-V_B) / (R_L + R_D) \tag{21}$$
$$V_{ss} = (R_D V + R_L V_B) / (R_L + R_D) \tag{22}$$

The undefined parameter t_0 can be estimated by $t_0 \approx d / v_{sat}$ where d is the device thickness and v_{sat} is the carrier saturation velocity. These formulae provide the device voltage and current, from which the average longitudinal electric field can be inferred. The above Eqs. (16)-(22) describe the overall temporal behavior of the Geiger discharge; notice that the gross electrical behavior is essentially non-random in steady-state operation. This lack of randomness distinguishes the Geiger mode from the linear mode of operation of the avalanche photodiode. To proceed with a description of heating, a more detailed spatial characterization of the current density is needed to solve Eq.(7) and is as follows.

The steady-state breakdown current I_{ss} is given by $(\rho_h v_h - \rho_e v_e)A$, where A is the area of the breakdown and $\rho_{e,h}$ are the electron and hole densities, respectively, with mean velocities $v_{e,h}$. Electrons are the dominant ionizer and both electron and hole velocities are saturated at roughly $v_{sat} = 10^7$ cm/sec in silicon in breakdown fields.[2] To maintain a steady current in an avalanche started by one electron, there must be a sufficient number of carriers within the avalanche volume for the avalanche to regenerate itself: a large number of electron-hole pairs must be generated in order for a single hole, with its much lower impact ionization coefficient, to re-start an electron avalanche. This minimum number of carriers, G, both holes and electrons, may be inferred from the fact that the minimum device current needed to maintain breakdown is about $I_{min} = 50$ microamperes.[12] Setting $Gev_{sat}/\Delta z_B$ to this minimum current yields a value of G of about 6000, which is not inconsistent with direct measurements of the gain at breakdown.[11] The corresponding critical density is $\rho_{emin} = G/(\Delta z_B \Delta w_B^2)$, where G is the mean photoelectron gain in an avalanche initiated by a single electron, Δz_B is the thickness of the breakdown region and Δw_B is the mean width of the single-carrier-initiated avalanche. From the manufacturer, Δz_B is about 2 microns.[11] The width Δw_B must be of the same order, because the carrier's transverse velocity must be less than its saturated longitudinal velocity. Thus Δw_B is also about 2 microns, perhaps 1 micron for a full width at half max(FWHM). The minimum electron current density of $\rho_{emin} v_{sat}$ and an implied maximum breakdown area A roughly equal to $I_{ss} / (\rho_{emin} v_{sat})$. It follows that the maximum width of a single filament is roughly $(I_{sat} / I_{min})^{1/2}$. For example, if an overvoltage of 10 volts is used with a 50 kΩ series resistor and if the diode resistance is negligible, then the FWHM of the breakdown region is less than about 2 microns. Of course, this maximum radius must be achieved over time and undoubtedly carrier diffusion aids in increasing the radius of the discharge. Since diffusion sets a radius that grows in time like $t^{1/2}$, the above results indicate that the radius of the

discharge scales like $(I_{ss}t)^{1/2}$, i.e., like the cumulative charge. This qualitative scaling is successfully applied to the experimental results below.

It also follows that the location of the discharge is most likely to persist at the position of the initial avalanche, where the greatest number of avalanche-regenerating carriers are present. Furthermore, the avalanche is confined because of space-charge effects in cladding layers above and below the breakdown layer. This is because a typical APD will have an intrinsic layer both above and below the breakdown region and in this layer the carriers diffuses radially outward, which results in a charge density that reduces the voltage at both the breakdown site and in an annular surrounding region. The reduced voltage tends to suppress avalanches in the surrounding part of the breakdown region where there are fewer carriers anyway. At the voltages, currents and durations of interest, these arguments are apparently adequate to explain the radius of the breakdown filament—for higher voltages, larger currents and longer delays, other effects can become significant.[5]

This section summarizes the spatial and temporal behavior expected of an avalanche breakdown filament in silicon. The basic result is that a very thin line filament is predicted, with a FWHM of about 1-2 microns for the APDs under study, for the voltages, currents and load resistances of interest. The filament may persist for many nanoseconds in a quasi-steady-state condition, with a corresponding steady-state current and voltage.

3.4 NOISE SOURCES

Noise sources in the SLM arise from thermal generation of carriers, from spillover from one pixel to the next, spillover from one frame to the next or from optical imperfections.

The noise from thermal generation is easy to estimate. The noise for 0.5 mm device is about 300,000 per second for operation at room temperature and about 5000 per second at -25 C, based on actual measurements at the operating conditions of interest. If each pixel occupies about 6 microns and the device is square, there are about 6400 pixels on the face of the device. If the device is operated at 1 MHz with a duty cycle of 5%, then the corresponding noise per pixel per frame is 2.3×10^{-6} and 3.9×10^{-8} at room temperature and at -25 C, respectively. Operation at a slightly lower overvoltage could reduce the thermally generated noise significantly; operation at the manufacturer-specified overvoltage would result in a noise rate of about 1.9×10^{-9} or a bite error rate of 9×10^{-10}, accounting for 50% probability of the "on" state.

Another significant noise source is spillover. Spillover from one pixel to the next, referred to as parasitic avalanching, can occur from several sources: carriers can move from pixel to the next, secondary photoemission can travel from one pixel to another and heat can diffuse out from an active pixel.

Carrier diffusion is not thought to be significant if the device is properly designed because the carriers create a potential well around a breakdown filament that tends to suppress nearby avalanching.[5] Secondary photoemission is considered significant and is treated in detail in the next section. It's effect can be minimized by allowing some guardband around each pixel, by pulsing the voltage or by controlling the spatial deposition of current with pixellated electrodes or APDs or by using thinner APD structures. Parasitic avalanching is explicitly included in the following.

Spillover also comes from heat transfer. This effect is not expected to be important if the pitch of the pixel array exceeds about 6 microns, because as shown in section 3.2, less than 1°C of temperature change is caused at such large radii for the conditions of interest.

Spillover from one frame to another comes in the form of avalanche echoes. These echoes are presumably caused by decay of trapped carriers at energy levels within the bandgap. These trapped carriers are found to have lifetimes of about 70 nsec at room temperature,[12] though older devices at lower temperatures showed longer lifetimes.[5] The effect of these traps can be minimized by decreasing the frame rate. The effect of these traps are analyzed in Section 3.4.2. Their net effect is to increase noise by about 1%.

Cross-talk comes also from optical imperfections. Based on laboratory observations, this effect is not expected to be important for most applications. A last, obvious noise source at photon counting levels is shot noise. This noise source is easily analyzed by assuming the photons arrive with Poisson statistics.

Noise is characterized by the bit error rate (BER) or the signal-to-noise ratio (SNR). The BER can be computed in a straghtforward way for binary (on-off) operation, which is most natural for this device. The probability of error at a specific pixel is given by

$$BER = Pr\{ \text{ error } \} = Pr\{ \text{ avalanche at pixel | write beam off}\} \cdot Pr \{ \text{ beam off } \}$$
$$+ Pr\{ \text{ no avalanche | write beam on } \} \cdot Pr \{ \text{ beam on}\}, \qquad (23)$$

where the write beam is assumed to be on or off with equal likelihood, as usual. The conditional probability for error, given that the write beam is on, is given by the probability that none of $n \approx 80$ incident photons cause an avalanche. If the photodetection probability is $\eta \approx 0.3$, the conditional probability is just

$$\Pr\{\text{ no avalanche } | \text{ write beam on }\} = (1 - \eta)^n \approx 4.1 \times 10^{-13} \tag{24}$$

This is the effect of photon shot noise on BER. The other conditional probability can also be evaluated; it is given by

$$
\begin{aligned}
\Pr\{\text{ avalanche at pixel } | \text{ write beam off}\} &= \Pr\{\text{ thermally generated avalanche}\} \\
&+ \Pr\{\text{ parasitic avalanche }\} \\
&+ \Pr\{\text{ avalanche echo }\}
\end{aligned}
\tag{25}
$$

The first probability, denoted p_{tg}, is on the order of 10^{-7} for a cooled device, as discussed above. The probability of a parasitic avalanche is evaluated in the next section. It is given by

$$\Pr\{\text{ parasitic avalanche }\} \equiv p_p \approx 1 - \exp[-(n_0 - 1)\gamma_0 t_{wr}] \tag{26}$$

where n_0 is the mean number of neighboring avalanches, chosen to equal 25 and γ_0 is the rate of parasitic avalanching and is equal to about 150 sec^{-1} as computed below. The relevant write-read delay is $t_{wr} \approx (1/2) \times 50$ nsec. The resulting error probability is about 4×10^{-6}, for a fully-utilized reach-through device. If this estimate is correct, then parasitic avalanching is the dominant noise source.

The probability of an avalanche echo in the duration of the write pulse is given by

$$\Pr\{\text{ avalanche echo }\} \equiv p_e = Z \exp(-t_f / t_{tc})[1 - \exp(-t_{wr} / t_{tc})] \tag{27}$$

where Z is the total probability of an avalanche echo, which is about 0.13 from published data,[4] $t_f \approx 10^{-6}$ sec is the interframe time and t_{tc} is the time constant for the trapped carriers in the diode, which is 70 nsec based on manufacturer specifications, as mentioned above. The resulting error probability from echoes is then about 2.4×10^{-8}.

The resulting expression for the bit error rate is then

$$\text{BER} \approx 1/2 \{ (1 - \eta)^n + p_{tg} + p_p + p_e \}. \tag{28}$$

For the parameters described above, the resulting bit error rate is about 2×10^{-6} and is limited primarily by the probability of parasitic avalanches, if the published data is correct. This error rate, though small, is relatively large for digital data processing applications. For such applications, current and voltage control can be used as discussed in Section 7.2.3. With utilization of such techniques, bit error rates of less than 10^{-12} are expected to be achievable. For example, if the voltage is pulse-biased just twice during the duration of the write beam at the equally spaced durations and the write pulse energy is increased to 300 photons on average, then the bit error rate is $1/2 \{3(1 - \eta)^{n/3} + (p_{tg} + p_p + p_e)^3\} \approx 9\times10^{-16}$, which is well below the commonly-accepted standard for BER for digital processing.

When the device is operating in Geiger mode, it is either on or off, so the bit error rate is an appropriate measure for noise. However, if the device's voltage is pulsed during a write cycle, then thermal heating accumulates in proportion to the number of cycles for which the device is triggered to the on state. This is discussed in more detail in Section 7.1.5. Then the accumulated reflectivity acquires some dynamic range and the SNR within this range is relevant. The expression for SNR is

$$SNR = <m> / Var(m)^{1/2} \tag{29}$$

where m is the number of detected photons. Of course, the SNR depends on the mean number of incident photons per pulse-bias cycle, n. In this case, the APD is triggered by an incident photon with probability $p_s = 1 - (1 - \eta)^n$ during one of N pulse-bias cycles. The noise processes are assumed to be statistically independent and independent of the photon-incidence process and the processes from one pulse-bias cycle to the next is assumed independent. Then the SNR is

$$\frac{\sqrt{N}(p_s + p_{err})}{\sqrt{p_s(1-p_s) + p_{err}(1-p_{err})}} \tag{30}$$

where

$$p_{err} = p_{tg} + p_p + p_e. \tag{31}$$

For example, the SNR for 10 pulse-bias cycles, with 10 photons per cycle and a false count probability of 10^{-3}, the SNR is about 17.9.

In summary, bit error rates are estimated for the PCSLM device. Bit error rates of about 4×10^6 are estimated with off-the-shelf parameters and this could be reduced to 8×10^{-12} with a simple

pulse-biasing technique and with write-pulse energies in the photon-counting range. Significant further reductions are expected with slightly more rapid pulse biasing or with thinner APD devices.

3.4.1 Parasitic Avalanching

Parasitic avalanching is an avalanche that develops at a second location as a result of an avalanche at a first location. It is caused by carrier diffusion and secondary photoemission. It is considered to be a potential noise source for multi-pixel operation of a spatial light modulator based on monolithic avalanche photodiode technology.

Parasitic avalanching caused by carrier diffusion is of minor significance for reach-through structures of interest here.[5] This leaves secondary photoemission as the source of parasitic avalanching. The following model is aimed at analyzing the strength of parasitic avalanching versus time as a consequence of secondary photoemission. The model is adaptable to a treatment of carrier diffusion as well, if needed.

A key assumption made by the model is that a certain minimum current I_{min} is needed to support a single breakdown filament. This assumption is based on documented electrical measurements.[12] This assumption is extended by positing that any breakdown filament consists of one or more minimal filaments, each of current I_{min}. Additionally, it will be assumed that each minimal filament is assumed to occupy an area A_{min} oriented transverse to the electrical field.

A parasitic avalanche is a random event; it depends on the probability that a carrier is produced; in this case a carrier is produced by random secondary photoemission. It also depends on the probability of breakdown, which depends on the external overvoltage $V-V_B$ and the current I available to support additional breakdown.

There are two physically different assumptions that produce different results. In the first case, the initial avalanches consume all of the available current; in the second case additional current is available to start new avalanches. The latter case includes the initial capacitive discharge of the APD. The first case arises when the number of avalanches has increased to the point where all available current is consumed. This case corresponds to the steady-state electrical operation of the diode circuit. In this case, a secondary photon may be emitted and absorbed, but an avalanche may not occur immediately after absorption if inadequate current is available to maintain its breakdown. Both cases can be described as Markovian random processes. These cases are treated separately;

the latter case is treated first because it is simpler, then the more relevant steady-state case will be treated in most detail.

Excess available current (transient electrical conditions)

It is desired to find the probability distribution of both initial and parasitic avalanches at time t. This distribution depends on the number and type of avalanches at prior times. The probability that there are n' initial avalanches and m' parasitic avalanches at time t', given that there are n initial avalanches and m parasitic avalanches at an earlier time t, is denoted by

$$\Pr\{ \ (n',m') \ \text{at} \ t \ '| \ (n,m) \ \text{at} \ t\}. \tag{32}$$

Consider a small time interval $t-t' = dt$; then the above probability may be expanded out in a Taylor series in time and expressed in terms of the various physical processes. Obviously, if the time interval dt is made small enough, then the number of initial and parasitic avalanches may each change by no more than one. Thus the only relevant probabilities are

$$\Pr\{ \ (n \ \text{or} \ n\pm1, \ m \ \text{or} \ m\pm1) \text{at} \ t+dt \ | \ (n,m) \ \text{at} \ t \ \}. \tag{33}$$

The probability of such events may be written, for example, as

$$\Pr\{ \ (n, \ m+1) \text{at} \ t+dt \ | \ (n,m) \ \text{at} \ t \ \} = \Pr\{ \ \text{a secondary photon is emitted,}$$
$$\text{\& secondary photon is absorbed at a non-breakdown site,}$$
$$\text{\& photon absorption results in a breakdown} \ | \ (n,m) \ \text{at} \ t \ \}. \tag{34}$$

The three composite events are physically and statistically independent and their probabilities are given by

$$\Pr\{ \ \text{a secondary photon is emitted in dt after t} \ | \ (n,m) \ \text{at} \ t \ \} \approx (n+m) \ \text{Imin} \ dt \ / \ Qo, \tag{35}$$
$$\Pr\{ \ \text{photon is absorbed at a non-breakdown site} \ | \ (n,m) \ \text{at} \ t \ \}$$
$$= \exp(- \ r/ \ r \ (\lambda)) \ (1- \ (n+m)A_{min}/A_{APD}), \tag{36}$$
$$\text{where} \ A_{min} = \pi \ r_{min}^2,$$
$$\Pr\{ \ \text{breakdown occurs at the absorption site} \ \} \equiv P(V-V_B) \tag{37}$$

Eq. (35) is based on experimental data, which indicates that a secondary photoemission occurs once for every 4×10^9 carriers that transit the APD, so $Q_o = 4 \times 10^9$ e in Coulombs, where e is the

magnitude of a charge carrier. The right hand side of Equation (36) is simply the product of the probability that the photon escapes the avalanche that produced it and that it arrives at a region that is not undergoing breakdown at time t. This depends on the radius r of the pixel, the absorption length $r(\lambda)$ of the emitted photon of wavelength λ and the fraction of the APD area, 1- $(n+m)A_{min}/A_{APD}$, that is not in breakdown. Equation (37) is based on the well-known APD property that the breakdown probability depends on the overvoltage $V-V_B$ applied to the APD. From Eqs. (35)-(37) one obtains an expression for the probability (34):

$$Pr\{ (n, m+1) \text{at } t+dt \mid (n,m) \text{ at } t \}.=$$
$$[(n+m) I_{min}dt /Q_0] \exp(- r/ r (\lambda)) (1- (n+m)A_{min}/A_{APD}) P(V-V_B) \qquad (38)$$

The probability (38) is then a differential probability, since it is seen to be proportional to dt. The remaining differential probabilities in Eq. (33) are all computed similarly. To compute all the needed differential probabilities, the probability is needed for termination of a filament avalanche. It is known that avalanche termination is an exponential process which depends on the current through the filament:

$$Pr \{ \text{avalanche i survives at least time t} \} = [1 - \exp(- I_i / I_{min})]^{t/t_{av}} \qquad (39)$$

where t_{av} is the transit time of a carrier, which is approximately equal to 40 picoseconds for devices of interest; I_{min} is the minimum filament current which is equal to about 50 microamperes for devices of interest. The expression (39) may be unfamiliar; to support its validity, the following brief derivation shows that it yields the correct dependence for the mean avalanche duration. Given a mean current I, the mean avalanche duration is equal to

$$<t> = \int_0^\infty dt \ t \ \ Pr \{ \text{avalanche i dies in time interval (t, t+dt)} \} \qquad (40)$$

where
Pr { avalanche i dies in time interval (t, t+dt) }

$$= \frac{d}{dt}[1 - Pr \{ \text{avalanche i survives at least time t} \}] \qquad (41)$$

and thus the familiar, experimentally-verified form for the mean avalanche duration is recovered, as given by Eq.(18):

$$< t \, (I) \, > \, = \, \frac{t_{av}}{-\ln(1-\exp(-I/I_{min})\,)} \; \approx t_{av} \exp(I/I_{min}), \qquad (42)$$

Equation (42) may be used to write Equation (39) in an especially simple form:

$$\Pr \{ \text{ avalanche i survives at least time dt } \} = \exp(- dt \, / < t \, (I) >) \qquad (43)$$

Thus Equation (43) is used to write the remaining probabilities, which are as follows:

$$\Pr\{ (n, m-1) \text{ at } t+dt \mid (n,m) \text{ at } t \} = 1 - \Pi_{i=1,m} \exp(- dt \, / < t \, (I_i) >) \,)$$
$$= m \, dt \, / < t \, (Imin) > \approx dt \, m \, \exp(-1) \, / \, t_{av} \qquad (44)$$

$$\Pr\{ (n-1, m) \text{ at } t+dt \mid (n,m) \text{ at } t \} = 1 - \Pi_{i=1,n} \exp(- I_i \, dt/ \, I_{min} \, t_{av} \,) \,)$$
$$= n \, dt \, \exp(-1) \, / \, t_{av} \qquad (45)$$

and

$$\Pr\{ (n+1, m) \text{ at } t+dt \mid (n,m) \text{ at } t \} =$$
$$[(n+m) \, I_{min} dt \, / \, /Q_o \,] \exp(- r/ \, r \, (\lambda)) \, (n_o A_{min} \, /A_{APD}) \, P(V-V_B) \qquad (47)$$

where $< t \, (I_{min}) > \equiv t_{av} \exp(1)$ is used and n_o is the number of initial avalanche sites at $t = 0$.

With Equations (38) and (44)-(47), all the relevant transition probabilities are defined for this Markovian process. In this case, excess current is always available to promote another avalanche. Therefore this case must terminate with a situation in which no excess current is available. This situation is the steady-state case treated next.

No excess current (steady-state electrical response)

In this case, no excess current is available, so that the total current, set by the external circuit, is $I = (n+m)I_{min} \equiv n_o I_{min}$ and an existing breakdown filament must "die" in order for a new filament to be "born". The probability (32) is now modified to include such a probability for a simultaneous birth and death of a filament in time dt. It is seen that the transition probability is of order dt^2 and thus any initial configuration of breakdown filaments are stable if current is strictly fixed. Since this is inconsistent with experimental observations, the steady-state-current assumption is modified slightly so that a filament may "die" some time before a new filament is

"born". With this assumption, a standard Markovian process is recovered with non-zero transition probabilities. For example, one of these transition probabilities is defined as follows:

$\Pr\{$ (n-1, m+1)at t+dt | (n,m) at t $\}$.=
   $\Pr\{$ a secondary photon is emitted,
      & same photon is absorbed at a non-breakdown site,
      & photon absorption results in a breakdown
      & an existing filament decays in dt | (n,m) at t $\}$ (48)

Given that a filament decay is statistically independent of the process of filament "birth", it is easy to show that the probability Eq.(48) is of order dt^2:

   $\Pr\{$ a secondary photon is emitted,
      & photon is absorbed at a non-breakdown site,
      & photon absorption results in a breakdown
      & an existing filament decays in dt | (n,m) at t $\}$ =
   $\Pr\{$ a secondary photon is emitted,
      & photon is absorbed at a non-breakdown site,
      & photon absorption results in a breakdown | (n,m) at t $\}$
   x $\Pr\{$ an existing filament decays in dt | (n,m) at t $\}$

This product of two probabilities can be written from Eqs.(38) and (45) above; the result is

$\Pr\{$ (n-1, m+1)at t+dt | (n,m) at t $\}$.
   $= [$ (n+m) I_{min} dt $//Q_o]$ exp($- r/ r (\lambda)$) (1- (n+m)A_{min} /A_{APD}) P(V-V_B) $] [$ n dt e^{-1} / t_{av} $]$ (50)

which is seen to be proportional to dt^2 as claimed above. It may be seen that all other probabilities in this case are also of the same order in dt. This implies that the steady state configuration is stable given the above set of assumption of constant current; this result undoubtedly is incorrect if only because existing avalanches are dying off. Then the constant-current constraint is no longer strictly binding, which is not physically impossible, provided that the constraint is non-binding only for a short duration or by a small amount. If this is assumed, then the non-zero transition probabilities of birth and death of an avalanche are

$$\Pr\{ (n_0\text{- } m, m\text{-}1) \text{ at } t+dt | (n_0\text{- } m, m) \text{ at } t \} = m \, dt \, e^{-1}/ t_{av}, \ m=1,2,...,n_0 \qquad (51)$$

$$\Pr\{ (n_0\text{-} m - 1, m) \text{ at } t+dt \mid (n_0\text{-} m, m) \text{ at } t \} = (n_0\text{-} m) \, dt \, e^{-1/t_{av}} \qquad (52)$$

$$\Pr\{ (n_0\text{-} m - 1, m+1) \text{ at } t+dt \mid (n_0\text{-} m -1, m) \text{ at } t \}$$
$$= [(n_0\text{-} 1) I_{min} \, dt /Q_0] \, \exp(- r/ r (\lambda)) \, (1\text{-} n_0 A_{min} /A_{APD}) \, P(V_{ss}\text{-}V_B)$$
$$= (n_0\text{-} 1) \, (1\text{-} n_0 A_{min} /A_{APD}) \, \gamma_0 dt \qquad (53)$$

where $\gamma_0 = I_{min} /Q_0 \exp(- r/ r (\lambda)) \, P(V_{ss}\text{-}V_B)$, where Vss is the steady-state voltage and is typically only a few volts. Analogous to (53) is the rate at which initial filaments increase:

$$\Pr\{ (n_0\text{-} m, m) \text{ at } t+dt \mid (n_0\text{-} m -1, m) \text{ at } t \}$$
$$= [(n_0\text{-} 1) I_{min} \, dt /Q_0] \, \exp(- r/ r (\lambda)) \, (n_0 A_{min} /A_{APD}) \, P(V_{ss}\text{-}V_B)$$
$$\equiv (n_0\text{-} 1)n_0 \, A_{min} /A_{APD} \, \gamma_0 \, dt. \qquad (54)$$

Also

$$\Pr\{ (n_0\text{-} m, m) \text{ at } t+dt \mid (n_0\text{-} m, m-1) \text{ at } t \}$$
$$= \Pr\{ (n_0\text{-} m-1, m+1) \text{ at } t+dt \mid (n_0\text{-} m -1, m) \text{ at } t \}, \qquad (55)$$

$$\Pr\{ (n_0\text{-} m+1, m-1) \text{ at } t+dt \mid (n_0\text{-} m, m-1) \text{ at } t \}$$
$$= \Pr\{ (n_0\text{-} m, m) \text{ at } t+dt \mid (n_0\text{-} m -1, m) \text{ at } t \}, \qquad (56)$$

Note the special case in which $n_0 = 1$. In this case, if the current turns off, it stays off. This is because the probabilities of birth, (53) and (54), are zero. This is in accord with the well-known meta-stable behavior of Geiger-mode APDs.

The Markov equations implied by (51)-(56) can be solved for a case of special interest: the case when there are initially no parasitic avalanches, as may occur near the beginning of breakdown cycle. One may compute the probability of zero parasitic avalanches, given that there are initially zero parasitic avalanches and no initial desired avalanches. Thus the initial condition is

$$\Pr \{ (n=n_0, m= 0) \text{ at } t = 0 \} = 1, \qquad (57)$$

and all other probabilities are zero. The desired probability is

$$\Pr \{ m= 0 \text{ at } t > 0 \} = \Pr\{ (n=n_0, m= 0) \text{ at } t \} + \Pr\{ (n=n_0\text{-}1, m= 0) \text{ at } t \} \qquad (58)$$

where

$$Pr\{ (n=n_o, m= 0) \text{ at } t \} = \exp(- n_o t\, e^{-1}/ t_{av}), \tag{59}$$

$$Pr\{ (n=n_o-1, m= 0) \text{ at } t \}= \{ \exp [- n_o t\, e^{-1}/ t_{av}] - \exp[- (n_o- 1)\, \gamma_o t] \}/ (1 - \varepsilon), \tag{60}$$

and

$$\varepsilon = (n_o- 1)\gamma_o / (n_o\, e^{-1}/ t_{av}) \tag{61}$$

It should be noted that equation (60) applies when ε is much less than 1, usually $\gamma_o \approx 10^2$ per sec and $\varepsilon \approx 2 \times 10^{-7}$ for a single avalanche in a 40 micron reach-through structure. From Eqs.(58) to (61) one writes the desired probability:

$$Pr \{ m= 0 \text{ at } t > 0 \} = \{ \exp[- (n_o- 1)\, \gamma_o t] - \varepsilon \exp [- n_o t\, e^{-1}/ t_{av}] \}/ (1 -\varepsilon) \tag{62}$$

$$\approx \exp [- (n_o- 1)\, \gamma_o t] \text{ for } \varepsilon \ll 1 \tag{63}$$

The probability (62) is seen to have a simple form when the relevant approximations are used. If this probability is close to one, then parasitic avalanching is not a problem. For a electrical duration of $t=25$ nsec and $\gamma_o \approx 10^2$ sec^{-1}, the resulting probability of a parasitic avalanche is about 2.5×10^{-6} for a single avalanche. Since this probability is close to zero, then the probability of 1 parasitic avalanche is much larger than the probability of 2, 3, etc. avalanches and the mean number of parasitic avalanches, $< m_p >$, is then equal to

$$< m_p > = 2.5 \times 10^{-6} \tag{64}$$

The above results give the differential probability transition matrix for the case of nearly steady-state current. The process is in fact a Markovian process with non-zero transition probabilities, as in the previous case. The results indicate, as expected, that parasitic avalanching can be a major contributor to bit error rate.

3.4.2 Avalanche Echoes

It is well-known that trapped carriers play a role in setting the dead-time of an APD operating in Geiger mode. Given that trapped carriers may arise, they form a reservoir of potential breakdown sites. In this case the transition probability depends on the total number of trapped carriers, assumed to arise from secondary photoemission that was absorbed yet failed to avalanche immediately. The process in this case can again be made Markovian by augmenting the state vector

with the number of trapped carriers, c. The probability of decay of one of these c carriers in a short time dt is reasonably assumed to be negative exponential in time with time constant of roughly $t_{tc} \approx 70$ nsec.[12] The probability that the trapped carrier does not decay in time dt is then

$$Pr\{ \text{ trapped carrier does not decay } \} = \exp(-dt / t_{tc}) \tag{65}$$

This implies that the probability that one of c carriers does decay in time dt is

$$Pr\{ \text{ c-1 at t+dt } | \text{ c at t } \} = 1 - \Pi_{i=1,c} \exp(- dt / t_{tc}))$$
$$= c \, dt / t_{tc} \tag{66}$$

and this in turn is the probability that an avalanche is "born", given c trapped carriers:

$$Pr\{ (n, m+1, c) \text{ at t+dt } | (n,m,c) \text{ at t } \} = \text{(from Eq. (38))} \tag{67}$$

$$Pr\{ (n,m-1,c) \text{ at t+dt } | (n,m,c) \text{ at t } \} = \text{(from Eq.(45))} \tag{68}$$

$$Pr\{ (n-1,m,c) \text{ at t+dt } | (n,m,c) \text{ at t } \} = \text{(from Eq.(46))} \tag{69}$$

$$Pr\{ (n+1,m,c) \text{ at t+dt } | (n,m,c) \text{ at t } \} = \text{(from Eq.(47))} \tag{70}$$

$$Pr\{ (n+1,m,c-1) \text{ at t+dt } | (n,m,c) \text{ at t } \} = (n_o A_{min}/A_{APD}) \, c \, dt / t_{tc} \tag{71}$$

$$Pr\{ (n,m,c + 1) \text{ at t+dt } | (n,m,c) \text{ at t } \} =$$

$$= [(n+ m) \, I_{min} \, dt / Q_o] \exp(- r/ r(\lambda)) (1 - (n+m)A_{min} /A_{APD}) (1- P(V_{ss}-V_B)) \tag{72}$$

Again a Markovian process is obtained. Further analysis for this case will be deferred until deemed necessary, since published results are available.

3.5 OTHER OPTICAL EFFECTS AND OTHER MATERIALS

There are many means for modulating light in silicon; these are reviewed in Reference 22. In addition to the thermo-optic effect studied here, light can be modulated in pure silicon by free-carrier refractive-index and absorption and to a lesser extent by the Kerr effect, electroabsorption, electrorefraction and luminescence. Compound materials of Si and Ge exhibit other or enhanced

effects and engineered structures, e.g., quantum wells and electromechanical structures, offer significant advantages in some applications.

In silicon, several alternative types of silicon electrooptic modulators have been suggested.[22] These include depletion-type plasma devices, which have been demonstrated in this effort, as well as Pockels-effect modulators and electroabsorption field-effect modulators in quantum-confined structures. The plasma-type devices are compared below with other effects and are potentially useful in simple planar array structures. The Pockels effect is absent in pure silicon, but is present in the silicon compounds β-SiC and SiGe, with figures of merit $\Delta n/E$ of 25.7 pm/V and 184 pm/V, respectively. The third type of device suggested, based on electroabsorption, would utilize SiGe materials with strained-layer quantum wells. These devices are in their infancy and the diversity of possibilities in terms of materials and parameters precludes a thorough assessment of the potential performance of these quantum-well devices.

Another unique spatial light modulator based on silicon invokes micro-mechanical motion.[25] A silicon nitride film is deposited over a trough and when an electric field is applied, the film bends into the well, diffracting and delaying the light. The troughs are 1-2 microns in size and several troughs are combined to form a resolution element that is about 25 microns in size. This approach has demonstrated 25 nsec response time as well. This is an electrically-addressed device, not an optically-addressed device.

Other materials such as GaAs also have similar optical properties, but moreover, has a non-zero Pockels coefficient. Recent advances in spatial light modulation have utilized GaAs quantum-well structures in conjunction with an external electrical field to modulate the absorption of excitons at energies via the Stark effect on the energy levels of the well. The excitons are created by a writing beam and forms a state of definite energy, which absorbs light at a definite energy. If an incident photon is tuned to this energy it will be absorbed and if an external field varies the excitons' absorption energy, the absorption of the incident read-out light can be controlled. This approach gives a relatively strong and fast absorptive response compared to other approaches. Modulation has been measured at 1.1% at 100 kHz with 2.6 micron pixels, in a grating geometry.[24]

A plethora of other means are available for modulating light in GaAs-type materials, but more importantly, light can be created as well. The advent of "smart pixels" integrate a detector and an emitter together, so that the pixel is a strong source of light; approximately 100% contrast modulation can be achieved with this approach and an integrated detector/transmitter requires about

100 pJ / bit, operating at about 1 GHz.[25] The merits of this approach must be weighed against the poor spatial resolution, extensive fabrication and associated costs of the complex semiconductor structure.

To limit the scope of this survey, it is reasonable to focus on processes that are similar to the device developed herein. The device basically modulates light with light, using a carrier avalanche to enhance its sensitivity. Second, a very simple, inexpensive semiconductor structure is used. The strengths of the device are its photon-counting optical sensitivity and its 6 micron resolution. Further advantages of the device are its ease of manufacture and low cost, 100% optical fill factor and self-pixellation of the response. These features should be maintained by looking at basic effects that can be enhanced by an avalanche in familiar semiconductor materials.

There are several main disadvantages of the present device. First, despite the fact that the avalanche process has a time constant of about 20 picoseconds, the thermo-optic effect is relatively slow, with a time constant of about 50 nsec for reach-through structures. This is the time it takes for the induced modulation to diffuse away. This is expected to be a drawback in any high-resistivity avalanche device, but is minimized in materials that have high thermal conductivities. A shallow-junction device also reduces the voltage and power requirements and also the time it takes for heat to diffuse out of the device. However, it also reduces the amount of desirable phase modulation. Another problem with the thermo-optic effect is its electrical power consumption, which is about 4.0 nanoJoules per bit. This is not excessive, but is not competitive with other devices, such as smart pixels, which can operate in the 200 pJ/bit range. This problem can be eliminated by going to effects that couple electrical energy more efficiently to an optical wave or are of faster response.

A second drawback is that the device uses an asymmetric Fabry-Perot cavity, for which the refractive index modulation depends on temperature, including ambient. This problem can be mitigated by going to a thinner structure or by using an effect that involves absorption, luminescence or diffraction. In fact, as long as a device is read-out with coherent light, tight tolerances on temperature and manufacture are needed. This is true even if absorption or diffraction are the basic modulating effects and is true as long as the light actually penetrates the front surface of the structure.

Based on these remarks, the field of optical effects of interest are limited to common avalanche materials - GaAs or InGaAs as alternatives to Si. Recovery times are set by the most lingering effect, which is typically thermal. The table is limited to common, experimentally observable

effects. These considerations lead to the following Table 1. Based on this table, which neglects cost, smart pixels in GaAs have the speed and contrast modulation that are most appropriate for modern digital applications. For applications requiring a coherent read-out wavefront or very high sensitivity, the thermo-optic effect appears best and might be slightly better in GaAs than in Si, though the energy-bandwidth product is about the same for the two materials. The free-carrier effect might have merit in applications where fast framing is required with coherent wavefronts.

3.6 THEORY SUMMARY

The theory of the thermooptic effect in avalanche photodiode structures predicts temperature rises of about 6 K and corresponding reflectivity modulations of up to 80% for readily-available off-the-shelf devices, as shown in Figure 6. The theory is used for the comparison with experiment and will show good qualitative agreement. The relatively simple theoretical results presented above for the magnitude, speed and size of the thermo-optic response are qualitatively verified by experiment. The experiment is discussed in the next section. Predictions are also made for the magnitude and speed of the free-carrier induced refractive index.

The results in Figure 6 show about 74% modulation at the design point, assuming 10% reflectivity in the off-state. This compares directly with the experimentally-observed 32% modulation with 20% reflectivity, as is described in Section 4. It should be noted that the amplitude reflectivity is assumed to be 0.6 for both the front and back surface and further details of the calculation are given in routine pcslm.f included in Appendix B.

Corresponding to Figure 6 is a plot of spot size versus energy per bit. This plot, Figure 7, shows that the spot size varies little over the range of parameters of interest. A typical spot diameter (full-width at half max) is about 5 microns. At the design point the spot diameter is about 4.6 microns. This corresponds to an optical resolution of 217 line pairs per millimeter for the device. This prediction is in good agreement with the experimental results.

Bit error rates are estimated for a practical device as shown in Figure 8, based on published data for noise from thermal carriers, parasitic avalanches and avalanche echoes A noise avalanche probability of 10^{-3} is assumed; it corresponds to full utilization of the device surface area. Bit error rates of 2×10^{-6} are estimated for reach-through structures with the thermooptic effect and down to 9×10^{-16} with a simple pulse-biasing method. A design point is selected with 8 pulse-bias cycles per frame and 9 photons per pulse-bias cycle; this number of incident photons provide a 0.96 avalanche probability per pulse-bias cycle. This design has an SNR of 14 and a corresponding bit

error rate of 10^{-12}. Bit error rates of about 9×10^{-10} are expected from a similar analysis using the free-carrier effect.

Table 1. Prominent electro-optical effects in silicon and GaAs.

Silicon/ SiGe				
	Thermo-optic	Free Carrier[c]	Lumin-escence[d]	QW-Stark[h]
Op. Energy per bit (photons)	**10**	10	**10**	NA
El. Energy per bit (nJ)	**5.0**	1.2	**0.3x109**	NA
Max Contrast Modulation(%)	**80**	40	$\approx$**100**	NA
Rise time (nsec)	**18**	$< 1^f$	**< 1**	NA
Fall time (nsec)	10	$\approx 10^f$	**< 1**	NA
GaAs/InGaAs				
	Thermo-optic	Free Carrier[c]	Emission[g]	QW-Stark[h]
Op. Energy per bit (photons)	10	10	$\approx$**3x106**	**90,000**
El. Energy per bit (nJ)	1.1	0.32	**0.2**	NA
Max Contrast Modulation(%)	80	40	$\approx$**100**	**1.1**
Rise time (nsec)	18	< 1	**< 1**	**2000**
Fall Time (nsec)	40	$\approx$40	**<1**	NA

Table 1 notes:

[a] Numbers in bold have been experimentally anchored.

[b] Energy per bit = $c_p A \Delta z \ \Delta T$, where A = 16 μm^2, Δz = 4 μm and such that $\partial n/\partial T \ \Delta T = 0.002$. For Si, $\partial n/\partial T =$ 2×10^{-4} from Ref15. for GaAs, $\partial n/\partial T = 1.43 \times 10^{-4}$, from Ref. 26,p.432. c_p = 1.65 $J/cm^3/K$ for Si, $c_p \approx$ 1.97 $J/cm^3/K$ for GaAs. Thermal conductivity = κ = 1.48 and 0.37 W/cm/K, for Si and GaAs, respectively

[c] Magnitude of the free carrier effect from Fig. 10 of Ref.8 for Si,and scaled for GaAs based on an effective carrier mass of 0.07 me for GaAs vs 0 26 me for holes in Si. The free-carrier velocity was also needed for these computations, it is about 10^7 cm/sec for both Si and GaAs based on Refs 2 and 16, respectively.

[d] Magnitude of luminescence for Si based on Ref 7 # output photons / carrier = 2.5 $\times 10^{-11}$, with perhaps a factor of 10 higher actually generated. correcting for self-absorption. The luminescence in that experiment is broadband and was not observed for most of the diodes used in the experiments herein. The energy per bit has been chosen so that the same signal in photons (3×10^5)results as for the thermo-optic effect.

[e] See Reference 132 of Reference 22

[f] Speed of response based on free carrier transit time for 4 micron thick devices and assuming saturated carrier velocities. Fall time based on time for induced temperature variation to fall to T_f = 1 C:

$$t_{fall} \approx (c_p \Delta z^2/\pi^2 \kappa) \ln(T_{max}/T_f).$$

[g] Based on smart pixels in GaAs. see Reference 25.

[h] See Reference 24.
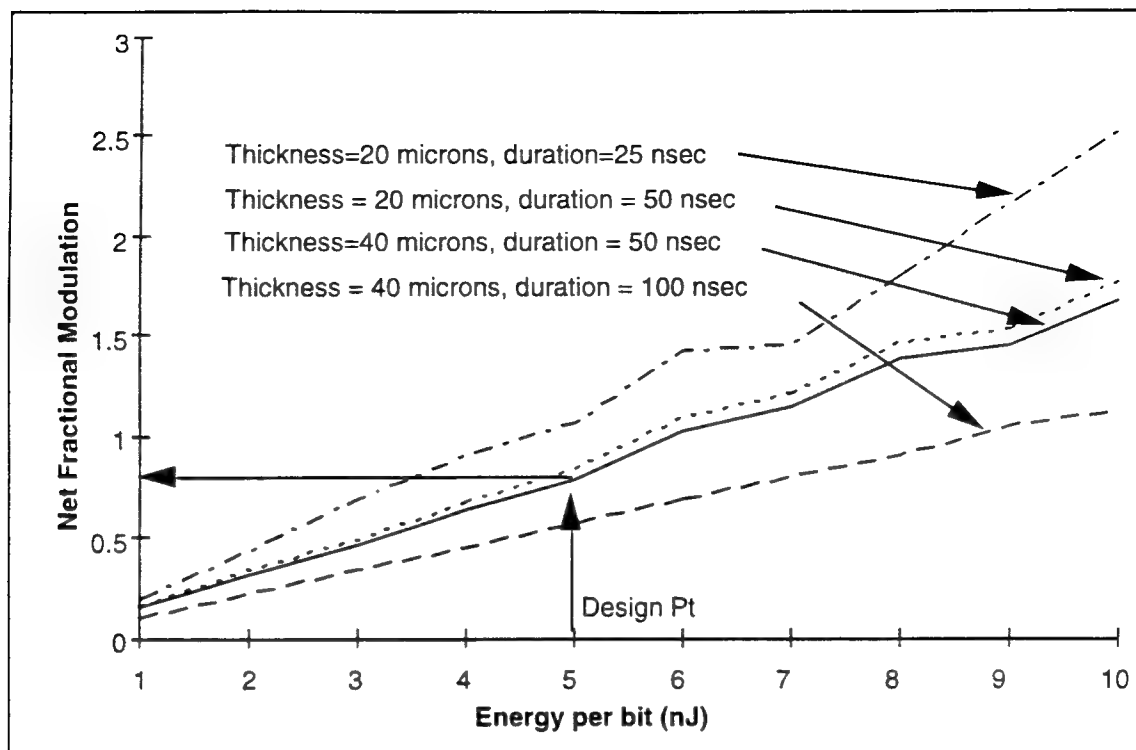
*Figure 6. Net fractional reflectivity modulation vs. electrical energy per bit.
Assumes 850 nm write/1300 nm read, 10% reflectivity in off state.*

The performance of the present approach is compared and contrasted with alternative state-of-the-art approaches for spatial light modulation. For digital applications that do not require spatial coherence, the GaAs smart pixel is superior because of the low energy requirements, high contrast modulation and high speed. Devices using quantum-confined electroabsorption are useful for applications at higher light levels and intermediate bandwidths when electrical energy consumption is constrained. For applications that require spatial coherence or high spatial resolution or high sensitivity, the thermo-optic effect in silicon or GaAs gives best performance. For applications that require coherence and frame rates in excess of about 100 MHz, the free-carrier effect in silicon or GaAs seems to show considerable merit because less energy per bit is needed.
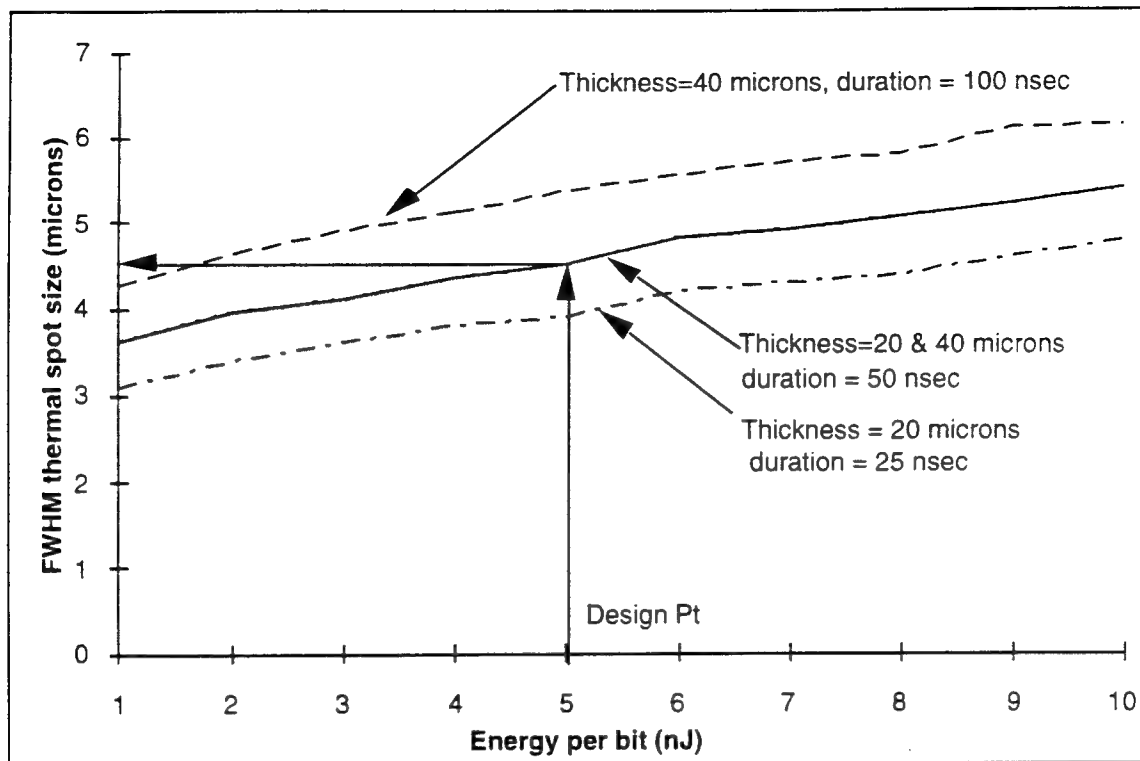
*Figure 7. FWHM reflectivity diameter (microns) vs. electrical energy per bit. Assumes 850 nm
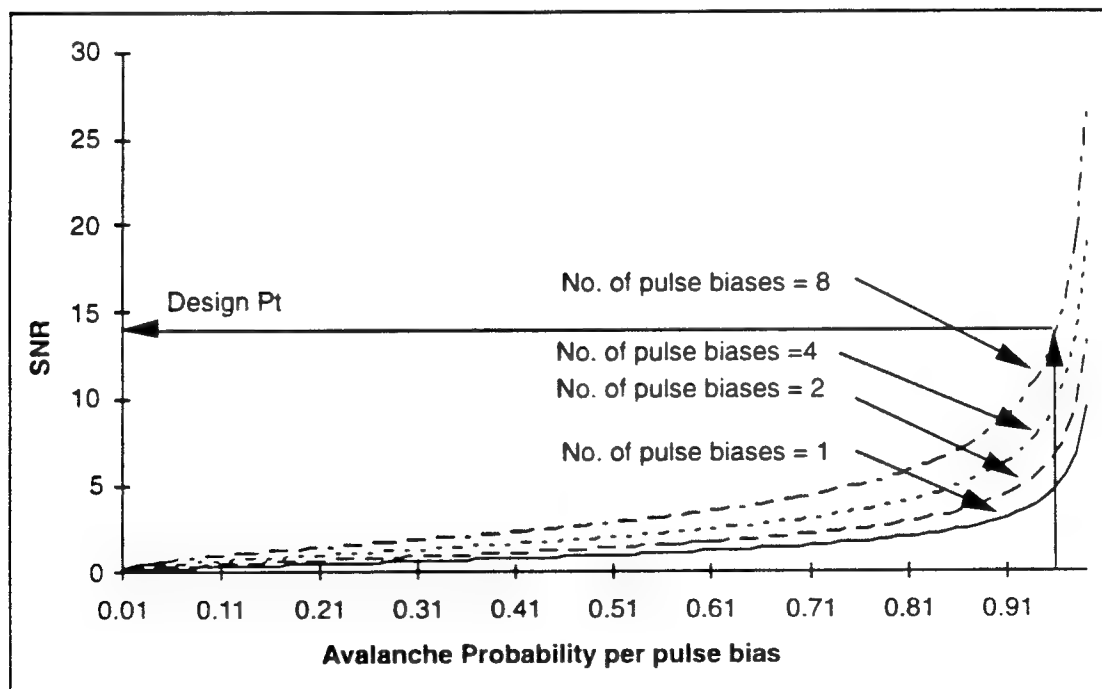write / 1300 nm read, 10% reflectivity in off-state.*

*Figure 8. SNR versus avalanche probability per pulse-bias cycle.
A noise avalanche probability per pulse bias cycle of 10^{-3} is assumed.*

4.0 EXPERIMENT

The lab setup is shown schematically in Figure 9. The setup is relatively simple. Optical paths direct light to the APD from the sources of read and write light and from the APD to a readout camera. The APD and 20x microscope objective lens are positioned to form a real image at the surface of the readout camera detector. Additional optical elements are needed to filter the spatial profile of the writing beam and attenuate its energy. The whole apparatus is put into a light-tight container to prevent excitation of the avalanche photodiode by stray light.
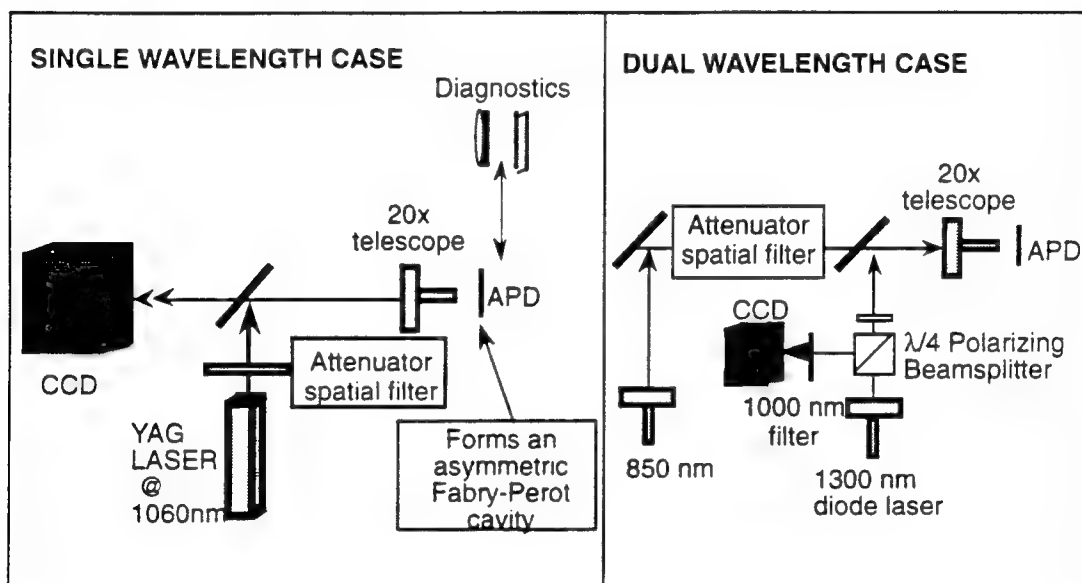
Figure 9. Schematic of the laboratory setup: (a) 1060 nm read/write; (b) 850 nm write/ 1300 nm read.

4.1 OPTICAL SETUP

Read and write lasers are directed through spatial filters and attenuators to a microscope objective. A 20x microscope then focuses the beams onto an avalanche photodiode. A fraction of the write light is absorbed, depending on its wavelength; light of 850 nm and 1064 nm wavelengths are used for writing. In the single-wavelength experiment, about 10% of the 1064 nm write light is absorbed and the reflected portion is used for read-out. In the dual wavelength experiment, the 850 nm light is completely absorbed (except for the small Fresnel reflection) and the 1300 nm light is used for read-out. The write beam is focused to a very small spot in order to insure that each avalanche is repeated in the same location. The write beam is spatially-filtered and attenuated to ensure the proper spot size and intensity. The read beam (if different from the write beam) is of larger radius at the APD in order to observe the spatial profile of modulation created by

the avalanche. The read beam is reflected from the APD back through the microscope objective and is then directed to a CCD camera. The face of the APD is imaged onto the CCD camera detector. Optical isolation of the CCD from stray reflections from the read and write lasers is ensured by direct observation and by insertion of a 1000 nm long-pass filter.

The delay of the read and write beam affect the strength of the optical modulation. The delays varied from 0 to 100 nsec. The write/read lasers operate at 20 kHz repetition rates. Consequently, the 30 Hz CCD camera averages over many such separate pulses to form an image, as shown in Figure 10. The experiment then compares the reflectivity of the APD with the write pulse triggered and not triggered. The difference in reflectivity may be ascribed to a change in the OPD of the device caused by the avalanche, provided several other experimental conditions are met as discussed below.
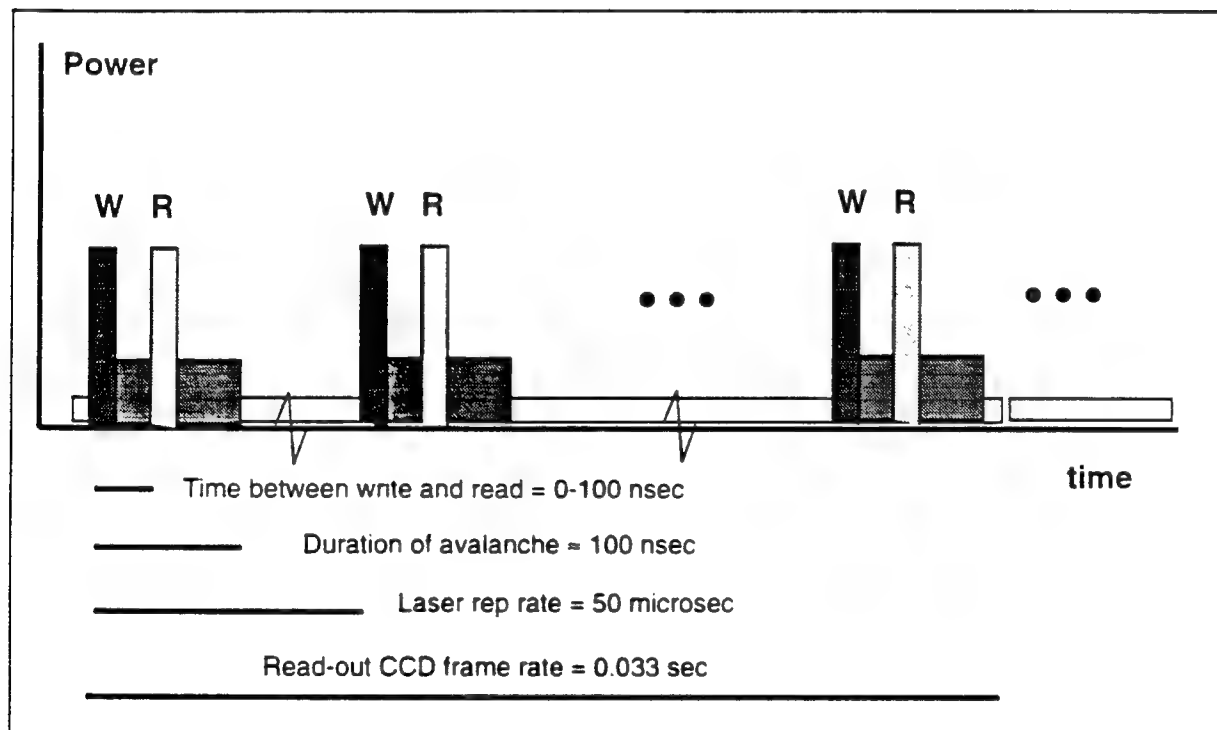
Figure 10. Timeline for the dual-wavelength experiment

Spatial filtering is needed to insure a small radius of the write light at the APD. A small radius is desirable for high resolution and useful for best response (larger spots require more heat to induce a given temperature change). Hence, substantial effort was spent to obtain a radius of about 2 microns for the writing light, as shown in Figures 11(a) and 12(a). A 20x microscope objective is used at the APD to accomplish this. The 1064 nm spots are about 4 microns FWHM and about

2 microns for the 850 nm reflection. These small spots deserve some explanation for the 850 nm case. The spots can be no smaller than the diffraction limit and should be somewhat larger because of expansion of the light over the depth of the diode. In fact, the latter enlargement is negligible for 850 nm light, because virtually all the light at that wavelength is absorbed within the first 5 microns of the device. Consequently, propagation through the full 35 microns of the device need not be considered. Thus the 850 nm spot is very nearly diffraction limited if the focal plane is imaged to the front surface of the APD.
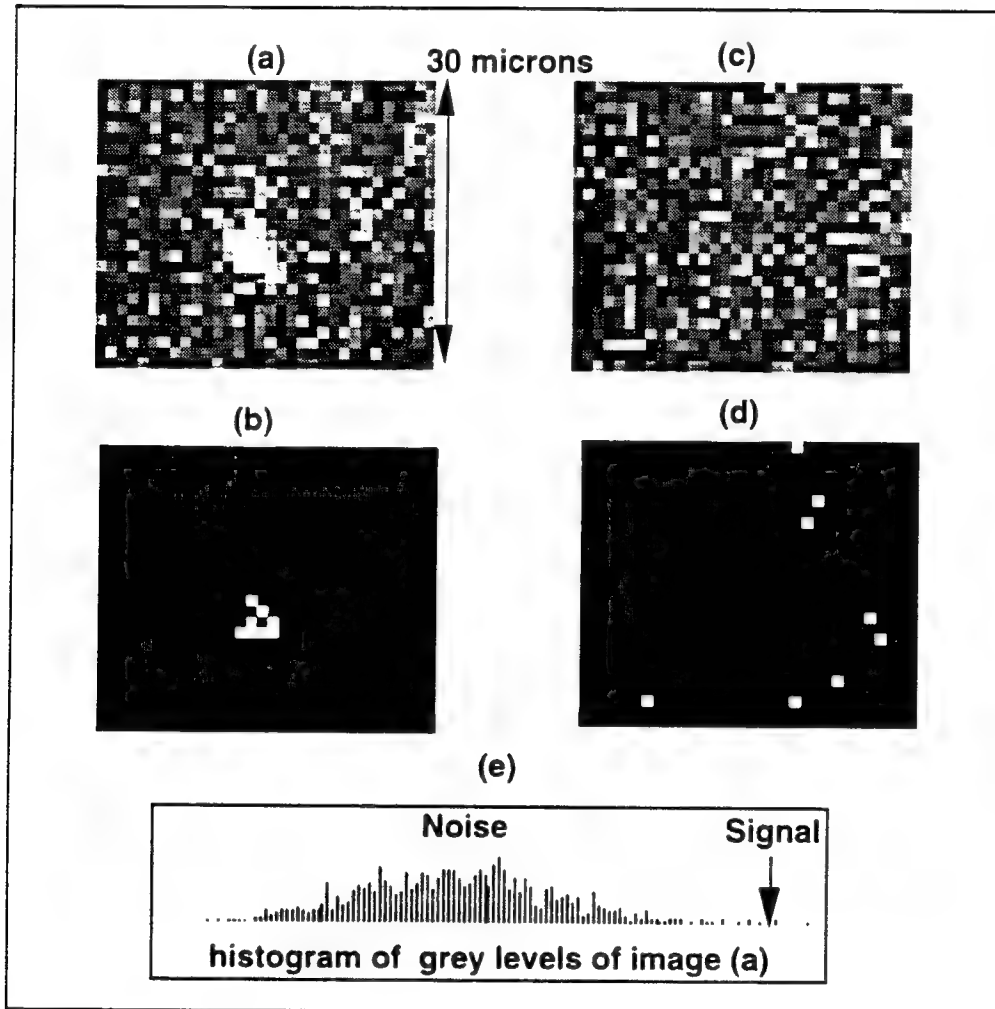
Figure 11. Evidence of excitation at photon-counting levels in 1064 nm write/read mode. The sub-figures in Figure 11 are as follows: (a) Subtraction of images with APD on and APD off; (b) threshold version of (a); subtraction of images with APD off; (d) threshold version of (c) at same threshold as (b); (e) histogram of gray levels of the image. The primary noise source is CCD camera readout noise.

The amount of light incident on the diode is controlled using an attenuator consisting of neutral density filters. These neutral density filters reduce the irradiance of the writing pulse to near-

photon-counting levels. In addition to attenuating filters, an important component of the optical train is the high-pass spectral filter in front of the read-out camera. This filter eliminates light below about 1000 nm and therefore eliminates secondary photoemission as well as the writing light at 850 nm. However, it passes the read-out light at 1300 nm.
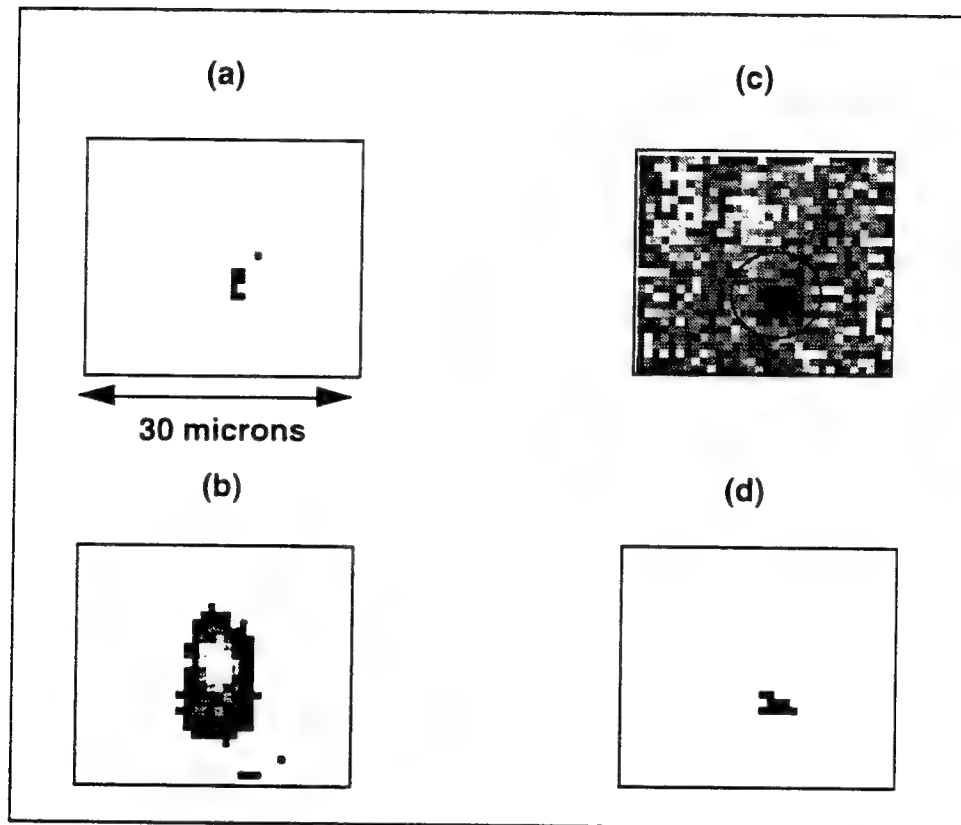
Figure 12. Evidence of excitation in dual wavelength mode. (a) Threshold image of the frame-averaged write beam (850 nm); (b) Threshold image of the frame-averaged read beam; (c) subtraction of read beam images taken with write beam on and off; (d) thresholded version of (c).

Substantial secondary photoemission is not observed externally when the diode is illuminated. None was observed outside of the excitation region. This was verified by camera and by eye. The presence of such emission should have led to a splotchy appearance on the camera or to an overall brightness increase. Furthermore, secondary photoemission occurs at wavelengths corresponding to energies greater than the bandgap,[7] and most of the experiments were conducted with a 1000 nm low-pass spectral filter in front of the read-out camera. Thus negligible secondary photoemission should have been observed in the data, as is the case. Internal secondary photoemission can cause secondary avalanches. These will increase the observed spot size and diminish the observed modulation since less current then flows through the initiating avalanche. Noise avalanches can

also result from thermally-generated carriers and from avalanche echoes. In this experiment, some low-level background modulation was observed at the higher overvoltages as seen in Figure 13(a). This may be attributable to such secondary avalanches.
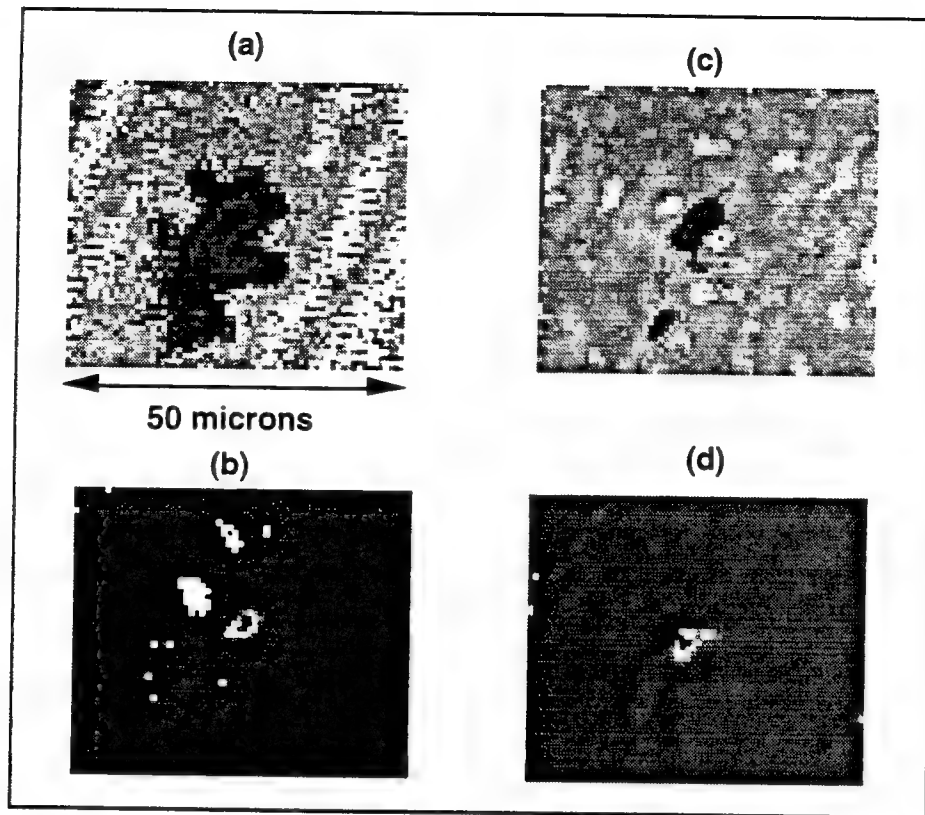
Figure 13. Summary data for the 850/1300 nm experiment. (a) Spatial profile of the read laser beam corresponding to (c), (b) Contrast modulation at an overvoltage of 10 V, load resistance of 50 kΩ and pulse delay of 96 nanoseconds; (c) Contrast modulation at an overvoltage of 45 V, load resistance of 50 kΩ and pulse delay of 58 nanoseconds; (d) Contrast modulation at an overvoltage of 20 V, load resistance of 50 kΩ and pulse delay of 96 nanoseconds.

The predicted heating is more than a few degrees Kelvin. This alone could cause an observable signal on the infrared-sensitive camera. However, calculations show that for the camera's spectral responsivity and for the expected change in emissivity of the APD, the direct blackbody response is negligible. This is verified experimentally .

Inter-frame heating is negligible. For the experiment described below, the frame rate is 20 kHz and the excitation time is only at most a few hundred nanoseconds. Quenching occurs from device heating if nothing else. Under these conditions, it is reasonable to neglect inter-frame heating.

Several potential sources of systematic error should be mentioned. First, the laser profile stability is good from one camera frame to the next, although an occasional overall shifting is noticed. Such overall shifts cause mis-registration, which causes characteristic light-dark patches in the differenced or ratioed frames. This effect can completely obscure the desired result and special care is needed to remove such registration errors.

Another potential error source is the spatial variation of the responsivity of both the APD and the camera. The former effect is not found to be significant. However, the camera read-out apparently causes ripple on some frames that made the data less useful. A last effect which could alter the measured response is diffraction of the read light within the APD. At the APD, the beam radius is very small and spatial variations in the beam can diffract quickly, altering the response in several ways. The best measured responses have been obtained when the spatial profile of the read beam is controlled to maintain a smooth profile. Given that an otherwise smooth profile is modulated by thermal effects, the spot radius is estimated from the modulation nearest the writing beam by averaging the half width at half max from the vertical and horizontal axes.

4.2 ELECTRICAL SETUP

The electronics of the sources and the APD are also important. A well-characterized off-the-shelf Geiger mode APD was used with a breakdown voltage is 245 Volts.[12] The APD power source is small—about the size of a cigarette pack. We use a PD-3 device, an off-the-shelf power supply available from Power Technologies. To obtain quickest, most uniform and most stable electrical response, the leads between the power supply and the APD were made as short as practically possible (about 2 cm in our case) and some care was taken in grounding the power supply. Specifically, we grounded the power supply through the same BNC cable which was used to examine the APD electrical signal output to avoid ground loops. To further stabilize the circuit and to provide passive quenching of the APD response, an additional load resistance is added. This resistance is varied to find best response; 50 kΩ seemed to be the right value. Larger load resistance results in less current and less heating in the APD. Smaller load resistance results in too much electrical jitter and allows excessive current to pass through the APD.

The power supplies for the light sources were triggered at 20 kHz and a variable delay could be introduced between the read and write beams with an accuracy of $\pm$ 1 nanosecond. The pulses themselves had FWHM durations of 10 and 14 nsec for the 850 and 1300 nm sources, respectively.

Another important feature of the lab setup is the configuration of the read-out camera. The read-out camera, a Teltron 1800, takes data at only 30 Hz, as shown in Figure 4-2. This would at first seem to be completely inappropriate for operation with the 20 kHz sources. However, the lower frame rate is actually beneficial because the signal is then integrated over many read/write frames of the PCSLM. This integration improves signal by a factor of 666, which is crucial in this low-light-level experiment and also insures that an average spatial response is obtained in the read-out image.

The photon detection probability, equal to the product of the quantum efficiency and the avalanche probability, has measured for incident light of wavelengths equal to 0.85, 1.06 and 1.3 microns. The measured values are 0.31, 0.01 and 3.9×10^{-9}, respectively, at an overvoltage of 5 V. Note the small detection probability for 1.3 micron light. This implies that the APD can be read without excitation using 1.3 micron light. Reading and writing can occur simultaneously with this approach, unless the 1.3 micron light is extremely powerful. If the 1.3 micron light is very bright or is over a large diode area, then delayed read-out may be used in conjunction with active quenching of the APD to eliminate triggering of the APD by the read beam.

Dark count can also reduce the measured response. If the diode is already triggered by a dark count when a writing pulse arrives, then the write-pulse will not excite the diode and the dark-count-induced avalanche will most probably be in a portion of the diode that is not interrogated by the read-pulse. Hence this will reduce the observed response. Based on manufacturer's specifications and data shown in Figure 14, this effect will reduce the measured contrast modulation by about 30% at the highest overvoltages, when operated at room temperature.
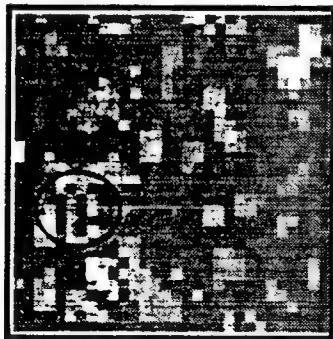
Figure 14. Improved contrast modulation
with optimized device

4.3 DATA REDUCTION PROCEDURES

When an image is obtained, it is stored. Later post-processing compares images with the APD voltage on and off and with the write beam on and off. The comparison involves subtraction or division of two images. This subtraction requires careful registration of the data between the two images. Independently, multiple background shots (APD voltage off) are compared to test consistency and statistical independence of the background. Both qualitative and quantitative comparison was performed. The qualitative comparison process consists of subtracting the gray levels of two images, subtracting the lowest resulting value from all pixels to reset the gray levels to positive values and then rescaling the image contrast to the full 256 gray levels. A similar rescaling was used for frame division. Sample results of such processing are shown in Figures 11 through 13. For the quantitative evaluation of the data, the gray levels were first converted to absolute irradiance using a manufacturer-supplied gamma curve, then nearest-neighbors smoothing was performed, followed by frame subtraction or ratioing.

The excitation was measured by both frame subtraction and frame division. The results are most clear when looking at the ratioed data. This suggests that read light is in fact modulated as given by the modulation factor of Eq.(1). If the excitation had been as evident with the subtracted frames, the response might be attributable to other effects, e.g., to direct blackbody heating from the thermal excitation. Furthermore, ratioing removes the effect of the read-beam intensity profile and this is desirable for accurate measurement of size of the spatial response.

Referring to Figures 11 through 13, which show the ratio of the read beam gray levels with the APD on and off, one clearly observes locations of modulation. At the highest overvoltages and longest delays, a low-level, large area modulation is observed. This is seen in Figure 13(a). Also, more background is observed in this figure as well because of the auto-rescaling of the camera and the processing, in accord with the reduced peak modulation that occurs in this case. These figures are useful in appreciating the quality of the data.

Several important overall observations should be noted. First, the contrast is not modulated unless an avalanche occurs—this is observed by turning off the 850 nm light when in dual wavelength mode. Second, the response for this part of the experiment is proportional to the deposited electrical energy and not the electrical current—this is found by varying the APD voltage and the read/write delay. If the contrast modulation were an electrical effect alone, the contrast would shift as the voltage was varied, even without an avalanche. This was not the case. Thus the observed effect requires the creation of an avalanche and has a dependence on voltage and time that

is consistent with the thermo-optic effect. The effect of plasma-induced refractive index modulation was observed at higher current levels with temporally-overlapping write and read pulses.

Data was taken at several different locations on the APD face. The reflectivity of the APD was observed to vary little within the central region within the central 90% of the diode. The modulation effect did not vary significantly, either, within this radius. This observation is qualitative and applies only to the diode under test and to conditions at which the data was taken. More quantitative and extensive variability measurements should be performed for characterization of devices for practical applications.

5.0 COMPARISON OF EXPERIMENT AND THEORY

5.1 PHASE 1

Qualitative images of the modulation are shown in Figures 11 through 13. The response is clearly visible and corresponds to $58\pm6\%$ modulation in Figure 11 for the 1064 nm experiment and to $32\pm7\%$ in Figure 12(b) for the 850/1300 nm experiment. A histogram of the image is provided in Figure 11 to better visualize the signal over the noise.

The results have been quantitatively reduced and are summarized in Table I. The theoretical reflectivities shown in the table uses the theory outlined in the section 3. The Equations (13)-(14) are used for the thermal excitation and the FWHM of the electrical excitation, $2r_0$, was set to 1.28 microns for an overvoltage of 10 V ($I_{ss} = 0.2$ mA) and a pulse delay, t, of 96 nanoseconds. The radius of the electrical excitation at all other overvoltages and pulse delays are scaled from this value using the $(I_{ss}t)^{1/2}$ relation posited in Section 3.3.

Several trends in the data should be discussed. First, the theory does offer substantial agreement with the experimental results. A second distinct trend in the data is that the reflectivity modulation tends to peak at an overvoltage of about 15 V and for intermediate delays. This might be counter-intuitive because the higher overvoltages and longer delays are just those for which the temperature shift should be largest. The result is easily explained, however, when one accounts for diffraction. When the temperature and phase shifts are large, diffraction is also largest and diffractive losses dominate, according to Eq. (5). The reduced response is also attributable to noise avalanches which draw current that would otherwise contribute to the desired effect. A third trend worthy of discussion is that the observed optical spot sizes actually decreased as the overvoltage increased. This probably has several causes. Strong defocusing occurs at the edge of the electrical discharge and this "throws away" read light that would otherwise be modulated. Diffraction is also thought to be responsible for the large variability in the experimental data at the higher overvoltages. Diffraction-ringing effects can cause both positive and negative spatially-varying reflectivity modulation. A better diffractive theory than the eikonal result of Eqs.(4)-(5) would undoubtedly aid in explaining the large spatial variation in the contrast modulation and would help justify smaller error bars. The smaller spot may also result from competing parasitic discharges at higher overvoltages that take away current from the primary filament—these reduce the current in the initiating avalanche under the steady-state current conditions used here.

Table 2. *Comparison between theory and experiment.*
Dual-Wavelength Experiment

Reflectivity Modulation (%)				
Overvoltage(V)	Read/write delay(nsec)	Experiment	Theory Fit	Opt.Radius(μm)
10	58	29 ± 7	25	3.3±1.1
10	96	32 ± 7	23	3.3
20	58	32 ± 16	28	2.5
20	96	18 ± 21	24	2.5
30	58	13 ± 19	18	2.0
30	96	11 ± 2	14	2.0
45	10	9 ± 2	12	<1.6
45	58	2 ± 27[1]	1.7	1.6
45	96	-1 ± 7[1]	-1.4	1.6
[1]Low-level, broad-area modulation was observed.				

A detailed comparison is not provided for the single-wavelength experiment because the size of the optical modulation could not be measured directly in that experiment. However, simple wavelength scaling from a read-out wavelength of 1300 nm to a read-out wavelength of 1064 nm predicts a contrast modulation of about 64%, accounting for off-state reflectivities 0.13 for the 1064 nm and 0.21 for the 1300 nm experiments. This is close to the modulation of about 60% that was observed.

The above summarizes the experimental parameters and results for the off-the-shelf APD. Of course, it is expected that an optimized device will do much better. Nonetheless, several practical issues remain for the characterization and manufacture of a useful device that is based on the avalanche-induced thermo-optic effect in silicon avalanche photodiodes.

For long-pulse case, it is noted that the electrical response is essentially the same as if a single photon were absorbed at the beginning of the read/write pulse, thus it is concluded that the observed contrast modulation is essentially the result of absorption of a single photon. It has been conjectured that repeated "seeding" of the excitation is needed to keep the avalanche localized, but evidence of this need has not yet been observed. It was not needed in the dual-wavelength experiment. The spatial distribution of the carrier current density may expand with time, but this did not seem to affect the basic experimental result.

The experimental results also have one other important implication. The refractive index profile diffracts light that is essentially lost. This loss can be considered a type of absorption, so the reflectivity modulation is less dependent on the optical thickness of the device and therefore is less sensitive to temperature-induced detuning thereof. These results of the first phase therefore bode well for a practical device in several respects.

5.2 COMPARISON OF EXPERIMENT AND THEORY-PHASE 2

This section summarizes results obtained in the second phase of the contract. Highlights of these results include improved contrast modulation to 80%, images with multiple pixels, an improved response time to 3 nsec with reduced contrast modulation and a precise measurement of the bit error rate for the device.

First, the reflectivity of the optically-optimized APDs are characterized. A batch of twelve of these ADPs were purchased from the manufacturer. The principal difference between the optimized devices and the off-the-shelf devices is that the front-surface anti-reflection coating was modified so that the front and back surface reflectivities are more nearly equal. The remaining uncontrolled free variable is the optical delay between the front and back surfaces and this variability led to a variability in the reflectivity of the device. Of the twelve devices, the device with the lowest off-state reflectivity was selected because it should give the largest fractional contrast modulations. The 1300 nm reflectivities of the twelve devices in the off-state is presented here.

<div align="center">

(1) 19%   (2) 23%   (3) 37.5%   (4) 22%   (5) 35%   (6) 25%

(7) 26%   (8) 24%   (9) 17.5%   (10) 21%   (11) 12%   (12) 12%

</div>

First shown are the higher contrast modulation results. The result shown in Figure 14 is obtained under conditions similar to that of the first phase of the experiment. An overvoltage of 15 Volts was used with a 40 nsec write-read delay with the optimized device near room temperature. Good results were also obtained by temperature tuning the unoptimized APD which had a thermoelectric cooler for temperature control. The figure clearly shows the high contrast modulation; the contrast modulation is measured at $78\pm8\%$.

The next measurement shown is the demonstration of high-speed modulation. For this measurement, the read and write pulses are shortened to 3 nsec FWHM and are overlapped in time. The load resistance is reduced to 5 kΩ, giving a total resistance of about 10 kΩ. An operating voltage of about 40 V was used, giving a current of 4 mA, which should result in a free-carrier

density of about 6.4 $\times 10^{16}$ cm^{-3}, assuming a filament size of 2 microns in width and a carrier saturation velocity of 10^7 cm/sec. The predicted phase change should be is given by $\Delta\phi = 2.2 \times 10^{-2}$ radians/mA. The off-state reflectivity for the optimized device is about 12% at room temperature, so inspection of Eq.(1) indicates that a phase change of about 0.022 radians should give at most a 7% change in reflectivity (from 12.0 to either 12.9 or 11.1% overall reflectivity). This is in relatively good agreement with the 8% that is actually observed, as shown in Figure 15. The contrast modulation is clearly visible in the difference between the read beams with APD on and off and the ratio of the two (after smoothing and removal of highest and lowest pixels in image) clearly shows the result as well.
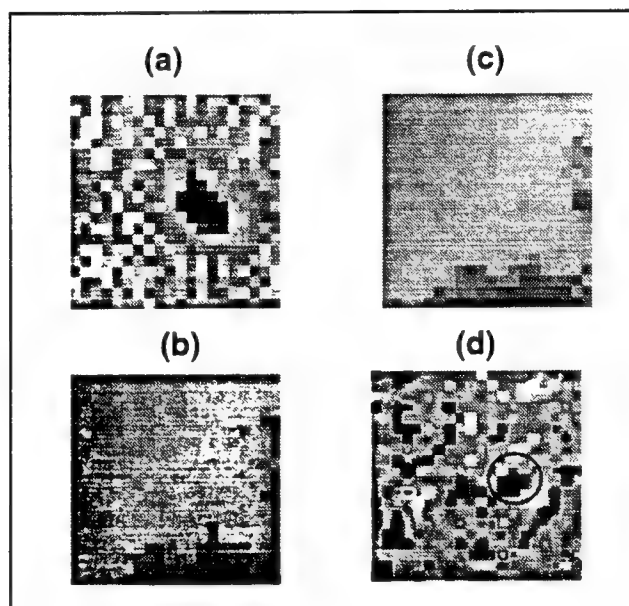
Figure 15. Contrast modulation @ 33 MHz.
(a) 850 nm write beam; (b) 1300 nm read beam with APD off;
(c) 1300 nm read beam with APD on; (d) ratio of (b) to (c).

Multi-resel images were also formed and observable modulation was found in this case too. A sample read-out image is shown, along with an image of the write beam in Figure 16. The image was taken with a 70 nsec electrical pulse duration and an overvoltage of 20 V. The write beam is at relatively high light levels. The read-out image is smoothed in post-processing to eliminate camera noise.

The bit error rate measurements are last. The dark-count induced error rate is shown first. This error rate is obtained by taking the total dark count rate multiplying it by the duty factor and dividing it by the total number of bits available per second. The duty factor is given by the on-time
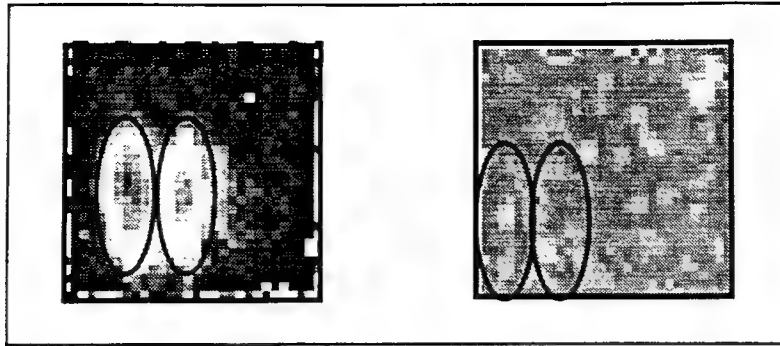
*Figure 16. Demonstration of multi-pixel operation with two pixels.
The left image is the write beam, the right image is the read-out beam.*

multiplied by the frame rate and is about 0.05 for a 50 nsec avalanche and a 1MHz frame rate. The total number of bits available is equal to the maximum number of frames per second, taken to be 1 MHz for this computation, multiplied by the number of 6 μm resolution elements in the 0.5 mm device. The result is a bit error rate of 3.5×10^{-6} bits per second at room temperature with an off-the-shelf reach-through APD structure. The bit error rate versus overvoltage, including error bars, is shown in Figure 17.
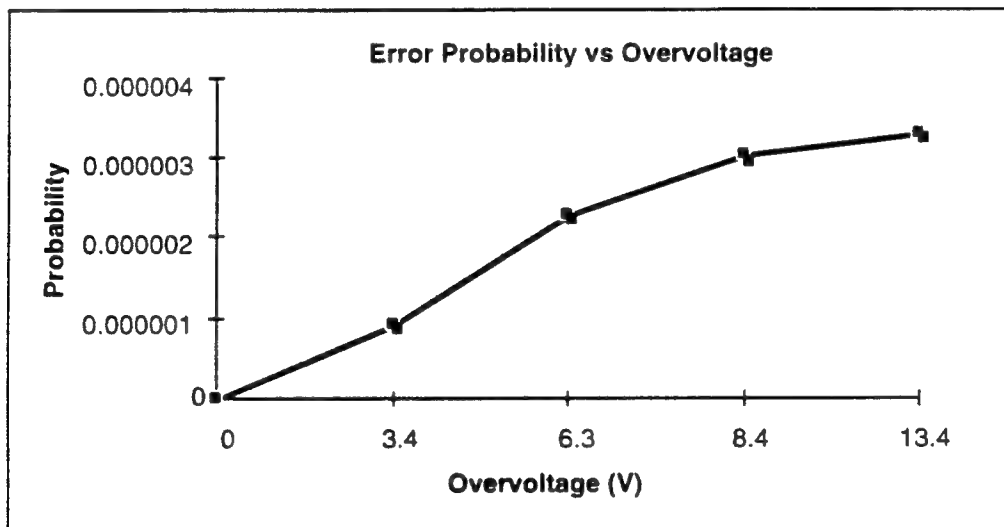
Figure 17. Error probability versus overvoltage.

In this experiment, attempts were made to measure the effects of avalanche echoes and parasitic avalanches. Both were not observable, however, because both derive from the number of avalanches written into the APD and at the low photon-incidence rates used here (20 Kcounts per second) and at room temperature, the dark count dominated these other effects.

6.0 APPLICATIONS

The possibility of localized modulation of light permits an application of the APD to spatial light modulation. The APD offers simplicity of manufacture, very high frame rates, very high resolution and very sensitive operation. Potential disadvantages are the high levels of power dissipation, the relatively slow thermal response and decay and the underlying temperature sensitivity. Several specific applications match the strengths of the approach yet do not stress its disadvantages; these include low-light-level spatial modulation, large-area optical switching and amplification, a display device, high-speed target identification, rapid optical beam steering and an optical serial-to-parallel converter.

A number of applications match the unique capabilities of the device. The photon-counting sensitivity of the device is comparable to that of electronic detectors, so low-light-level applications are an obvious match. These low-light-level applications include photodetection in astronomy and surveillance. In the latter area, the device is well-suited to work with near-IR laser radar.

Another low-light application is medical imaging. A detector that is sensitive at lower light levels also will require less dosage in a patient. If the device can be made sensitive to X-rays, then a very-low-dosage X-ray medical imaging system could be constructed.

The operation of the device allows a very intense read-out optical wave, if the APD voltage is quenched just before read-out. Operated in this fashion, the APD can act as an optical amplifier in which a weak wave controls a much stronger read-out wave, increasing the effect of the exciting photon by factors of 10^7. If sufficient current is provided to the device, then a single photon can switch the reflectivity of the entire area of the APD, so that the device acts as an large-area optical transistor with very high gain. Thus the device also can switch a relatively intense, large-area wave with a single photon. This implies an application in optical switching and optical communications. Furthermore, this same feature applied at the single-pixel level of processing implies that the device can act as a spatially-selective parallel optical amplifier, i.e., a parallel transistor. Because of the small effective pixel sizes and high frame rates, the potential throughput of the device is very high and an optical signal processing application is a possibility.

Individual pixels may be made into AND and OR gates simply by controlling the magnitude ΔV and duration Δt of a pixel's voltage bias and the pixel temperature. The voltage can be controlled on a pixel-by-pixel basis using active matrix addressing. The input-output characteristics of the device can be controlled by voltage as shown in Figure 18(a). The number of

absorbed photons in the write pulse are plotted on the abscissa. The contrast modulation of the write pulse is plotted on the ordinate. As more photons impose on a pixel, a proportional increase in current results if the device is near breakdown threshold. The increased current causes an increase in the temperature of the pixel. The pixel temperature increases the round-trip read-out phase, which in turn increases the amount of reflected read-out light if the Fabry-Perot cavity is tuned near null, as it should be for best contrast modulation.
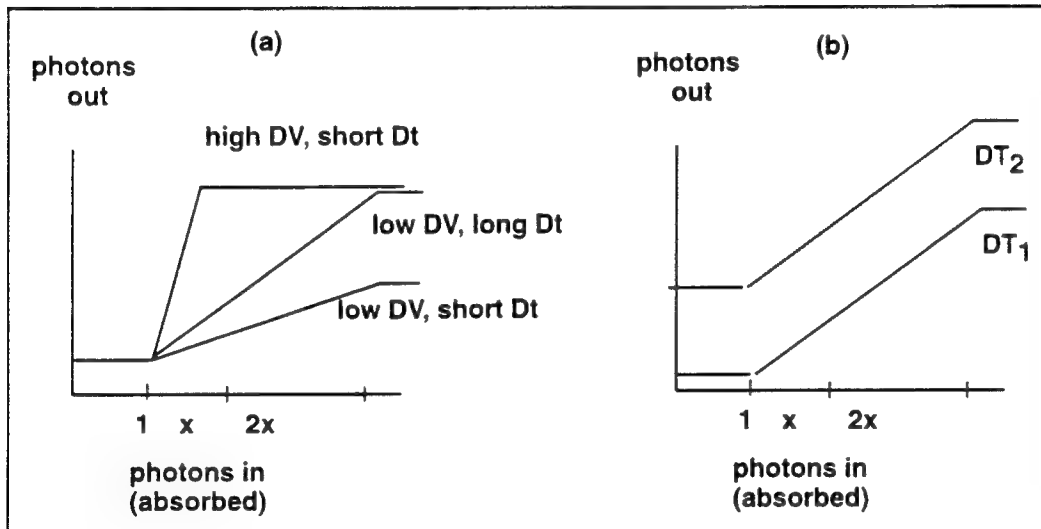
Figure 18. Control of the input/output characteristics of the device. (a) control of heat deposition by control of voltage ΔV and voltage duration Δt; (b) control of optical bias by control of temperature ΔT.

Accordingly, the pixel's temperature also affects the optical bias, as shown in Figure 18(b). The pixel temperature can be controlled on a pixel-by-pixel basis as well by pre-illuminating while a voltage is applied.

The result of these controls gives AND and OR gates as shown in Figure 19. Figure 19(a) shows off and on states for an OR gate that receives X photons in the "on" state. The corresponding voltage control is shown in Figure 19(b). The AND gate requires twice as many photons to be put into the on state, as shown in Figure 19(c). In this case, no temperature control is needed, only voltage control as shown in Figure 19(d). The AND gate has the same "on" and "off" contrast modulation outputs as the OR gate and thus allows binary optical states to be well-defined.
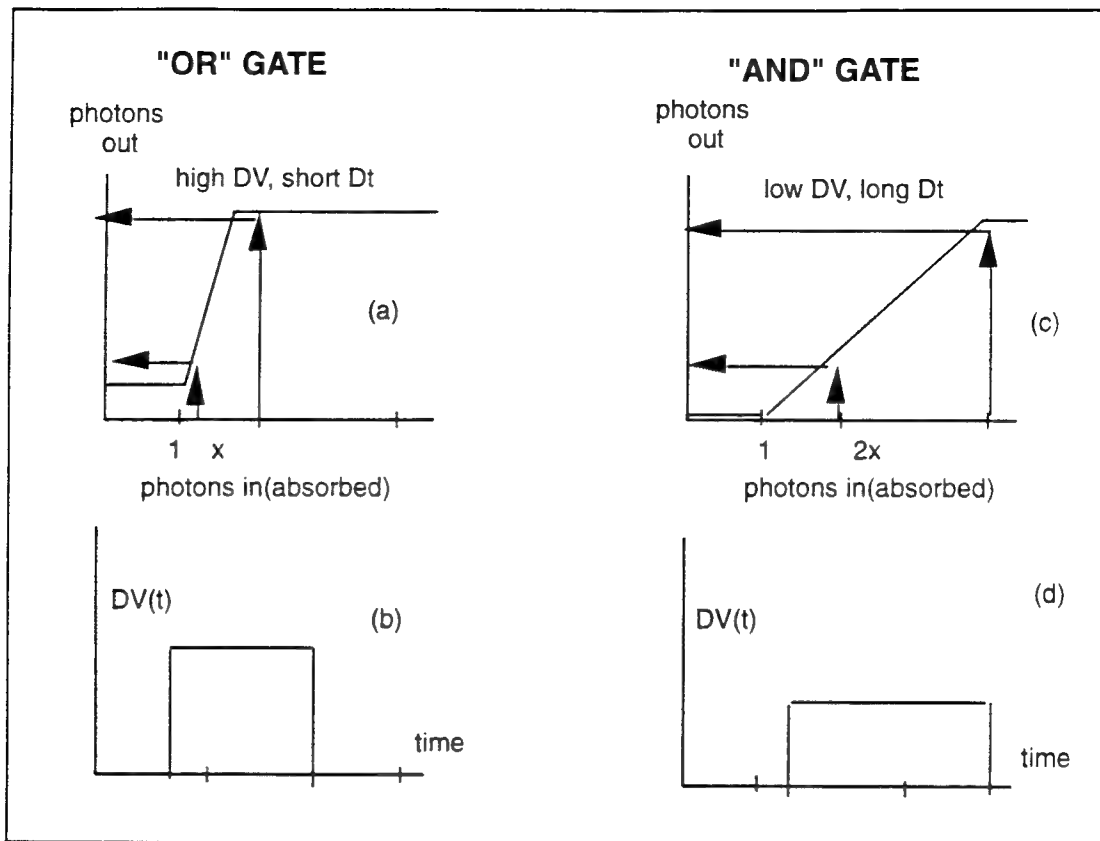
Figure 19. AND and OR gates by voltage and temperature control. (a) on and off states of OR gate; (b) corresponding schematic voltage control; (c) on and off states of AND gate; (d) corresponding schematic voltage control.

Display technology is another potential application. The high density of resels available with this technology might allow arrays of up to 800 x 800 resels to be addressed optically on a single APD that is about 0.5 cm in width. This and the potential low cost of the approach suggests that the APD might be useful as an commercial display device. For this application, the frame rates are relatively low (< 100 Hz), so power consumption and dissipation is not a problem. The main drawback of this approach for displays is that it reads-out most effectively in the IR. Read-out in the visible, however, is not precluded if the APD is designed properly. For example, a device that is 4 microns in depth will have a low quantum efficiency of only about 10% in the red and so would reflect about 40% of the incident light, accounting for transmissive losses and would be able to operate at only 25 Volts with the lower resistivity materials. Also, the APD would be electrically- addressed, not optically-addressed and could use passive-matrix fabrication techniques.

Of course, most displays operate with 100-micron sized pixels and a thermo-optic display device should be consistent with these sizes. To attain these large sizes, an alternative design and fabrication approach is needed, as shown in Figure 20. In this case, use of small, ≈20 micron, diodes would conserve electrical energy and mounting on a glass substrate would help hold the heat in the diodes for the longest possible refresh times. Presently available are microlenslet arrays with 100 micron diameter lenslets that are available in the visible that would produce 6 micron spots at the photodiodes. Multicolor operation would be achieved by temporal multiplexing. The device would operate in the projection/reflective mode. In this case, temperature control would be very important to maintain acceptably high contrast ratios. This fact and the complexity of manufacture suggest that this approach is not competitive with other technologies.
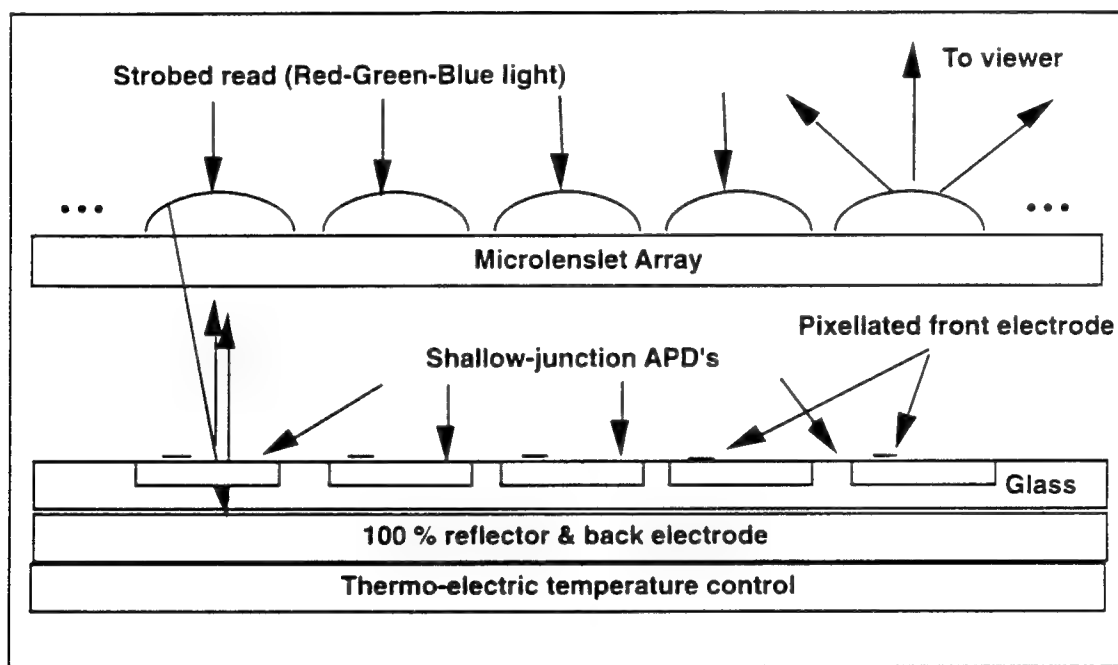
Figure 20. Schematic of a flat-panel display that operates in reflective projection mode.

Other aspects of the device are attractive for optical signal processing applications. The device is relatively easy to manufacture. The device does not require pixellation because the avalanche is self-localized to a few microns. It can be fabricated on relatively large areas and will operate effectively if the voltage is quenched before and after a write/read cycle. Furthermore, the response is both excited and read using optical means, allowing fast parallel access of the individual resels. Additionally, the APD will electrically stabilize in less than a microsecond and the heating will diffuse away within a fraction of a microsecond, based on the observed spot sizes and the thermal diffusion equation. Frame rates of up to 80 MHz should be achievable with this

device based on the internal heat dissipation limit. Single-pixel, shallow-junction APDs with 4 micron thickness should be able to operate at frame rates as high as 2 GHz with proper thermal engineering.

In our experiment, frame rates of only 20 kHz were observed because of speed limitations on the drivers for the read/write lasers.

The device can also be used for a serial-to-parallel optical converter. Its estimated total throughput of up to a Terabit/sec is capable of handling current and projected data rates of up to 100 Gbit/sec for a Wide Area Network (WAN). The thermal memory is an asset in this application because the serial bits must be buffered into the SLM. All bits in the frame are then read-out simultaneously and in parallel. An architecture for this application is shown in Figure 21.

Another important application of this device is rapid optical beam steering. The device should be able to steer over angle of up to 36°, based on a wavelength of 1.064 microns, a grating period of 6 microns and the refractive index of silicon. The approach should permit addressing over this field-of-view with switching rates of 1 MHz for the thermo-optic effect. Switching rates of up to 1 GHz are possible using the free-carrier effect with reduced diffraction efficiency.
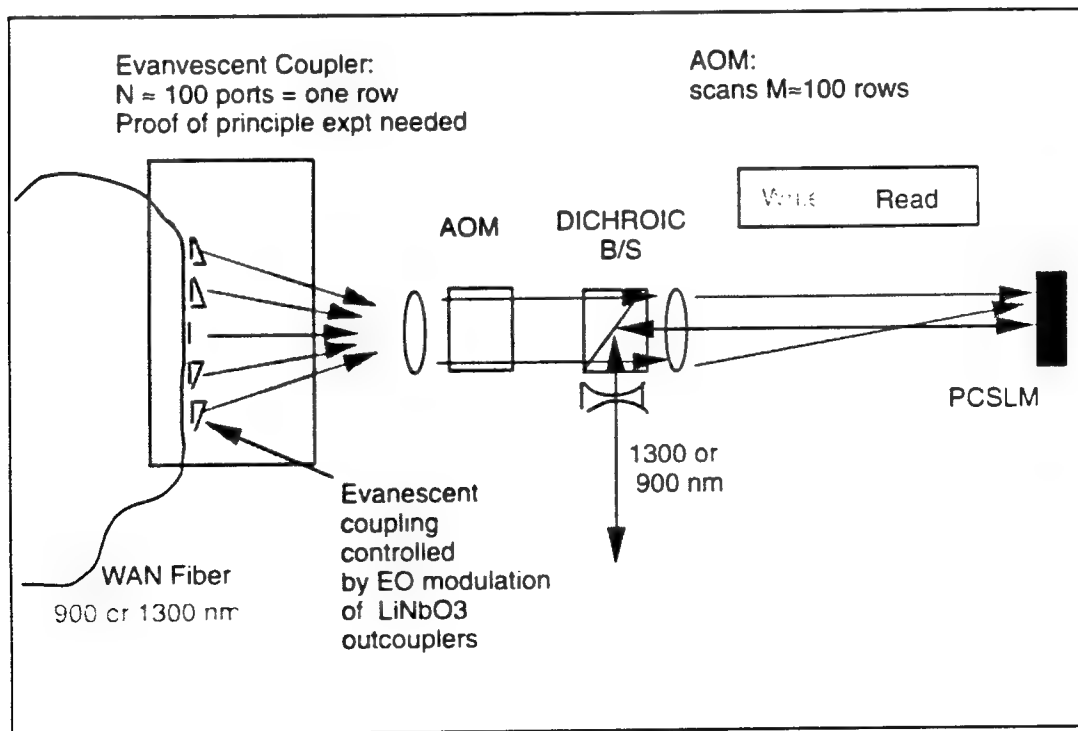

Figure 21. All-optical serial-to-parallel converter.

The device is extremely rugged and compact. Thousands of read/write cycles were performed at a single location on the diode, at voltages well above breakdown with no evidence of device failure. The off-the-shelf device itself is about 500 microns in size and the power supply used in the experiment is the size of a cigarette pack. Additionally, it is expected that the magnitude of the response will be quite uniform (low in noise) if proper electrical design is used.

The resolution of the device is quite good. Pixel diameters of about 6 microns have been observed and further reductions may in pixel size may be attained by using thinner devices. The overall device size is about 0.5 mm, but larger devices, up to 0.5 cm in width have been fabricated with comparable quality. Hence up to 800x800 pixels per frame are expected, with corresponding throughput in the Terabit/sec range.

The benefits for SLM operation must be weighed together with the aspects of the technology that have not been demonstrated. Foremost is thermal control and next is optical uniformity of manufacture. A third issue is scalability to shallow-junction devices while maintaining acceptable contrast ratio. Fourth and finally, although the overall pixel noise has been measured, the detailed spatial noise properties are difficult to measure directly with existing cameras because they have much higher noise than the device itself.

These features of the device, both demonstrated and projected, offer the potential for several specific applications of spatial light modulators. In particular, operation as a low-light level detector is an obvious possibility and an extension to target recognition. The high frame rate and resolution of the device make it attractive for high-throughput optical computers. The possibility of a large-area switch at low light levels could be useful for optical steering and amplification. And an optical serial-to-parallel converter is an obvious match with the speed of the device. The key potential benefit of the APD in any of these applications is its low cost. These and other features of the device must be quantified more carefully in order to determine the suitability of the device for the applications described; this is done in the next section.

7.0 DEVICE DESIGN

The device may be designed for any of a number of specific applications. These applications may be classed into two broad categories: (i) low-light-level applications, in which about 1 photon per frame is detected; (ii) spatial modulation applications in which many pixels are simultaneously excited per frame. The former category is easiest and is treated first.

7.1 LOW-THROUGHPUT OPERATION

Based on results obtained thus far, an optimized low-light-level device will not differ too much from the present EG&G reach-through structure. The electrical configuration will also be about the same as used in the lab. The primary changes needed for improved single-resel (resolution element) operation is a minor change of overall optical thickness and equalization of front and rear amplitude reflectivities at about 0.7. A thinner breakdown region and a thinner device are also helpful but unnecessary to create smaller resels; this would result in higher resolution, less electrical energy per resel and therefore also less power dissipation per resel.

7.1.1 Optical Specifications

The device is already near optimum for many applications, because of its relatively small resel area and high quantum efficiency. Optical optimization is needed to improve the contrast ratio between on and off states. To achieve a contrast ratio of 70 % out of a possible 100 %, two requirements must be met. First, the reflectivities of the front and back surface must be made more nearly equal. This was done in Phase 1 simply by removing the AR coating and using an SiO_2 front surface. Second, the optical thickness of the device must be chosen so that the front and back surface reflections are in destructive interference. This can be achieved most simply with an existing device - merely select an existing device with a thickness that is near a null and then tune to the null with temperature control. The optical thickness could be set in the manufacturing process and the usual process by which this is done, fluid-phase etching, is capable of etching to the desired tolerances of a few nanometers.[11] However the etching process is currently not controllable to such an accuracy and such heroic measures are unnecessary with temperature tuning.

The devices are relatively flat, so temperature tuning of an existing device will work over the entire face of a device, if the device is not too far from the desired thickness. The available amount of temperature tuning is about 10 K or about 0.7 radians of optical bias. The device thicknesses

are random and may be considered to be uniformly distributed over the range optical biases from 0 to 2π. Thus simple testing should yield suitable optical biases for about 11% (= $0.7/2\pi$) of existing devices.

Note that operation in reflection is preferred. The alternative mode of operation in transmission is not desirable because it halves the already relatively weak response and is mechanically fragile.

7.1.2 Thermal Specifications

In order to obtain adequate optical response, no more than 1 radian of phase change is needed. This in turn requires a localized temperature rise of about 10 degrees Celsius. To maintain about 10 % uniformity of response. It therefore follows that the temperature should be uniform to within 1.0 degrees Celsius of the nominal value, over the face of the APD. This rough rule of thumb is verified by more detailed analysis. This uniformity is is somewhat constraining; realistically, more flexibility will probably be needed for a commercial device.

Thermal control will not be needed for single-resel-per-frame applications, because the power dissipation rates are so low ($\approx$ 1 mW) that thermoelectric control is adequate.

7.1.3 Size Specifications

Given from Section 7.1.2 that the temperature should be maintained to within 1.0 degrees, one may deduce a corresponding thickness uniformity requirement. A 1 degree temperature change corresponds to about 0.08 radians of phase change. This phase corresponds to a thickness variation of about 5 nm over the surface of the device. This thickness tolerance is somewhat constraining. Contemporary manufacture of reach-through avalanche photodiodes typically have a uniformity variations of about 40 nanometers of thickness per millimeter width, comprised primarily of slope. Also, present techniques permit thickness measurements that are accurate to only about 100 nanometers. Given these facts, devices with the requisite uniformity can be manufactured in sizes of only 120 microns or less, for the thicker reach-through structure. State-of-the-art techniques using wet-etching and optical diagnostics can control thickness to the order of a nanometer, which could meet the 5 nm specification. It should be noted that epitaxial growth of shallow-junction structures also achieve this tolerance on thickness for devices sizes up to 0.5 cm and are cheaper as well.

Large area devices are acceptable, if flexibility in contrast ratio is allowed. Then the primary constraint is that only a small fraction of the available electrical energy should be drawn into noise avalanches. This implies devices of up to 0.5 cm in size (Ref. 18). The corresponding pixel array is about 800x800, assuming 6 micron pixels. However, if high contrast is to be maintained over the entire area, then current manufacturing techniques permit sizes of only the order of 120 microns or less, for reach-through structures. For epitaxially-grown device, on the other hand, more than adequate thickness control is available and devices up to 0.5 cm in size should be easy to fabricate. A device of this size is suitable for a number of potential applications.

The overall device thickness is an important parameter. A reduction in device thickness alters various properties of the device. It reduces the frequency of noise-induced breakdown, because less volume is available for thermal generation of free carriers. It may reduce secondary photoemission-induced avalanches, as discussed in the literature.[4,5] It will reduce the resistivity per unit area of the active device. This can also be viewed as a benefit. A thinner device will have somewhat more thermal conduction through the front and back surfaces, which can be viewed as a benefit for cooling in high-throughput applications. Such enhanced thermal conduction could also reduce the thermooptic response, although this should be of little importance for the selected pulse formats and reach-through structures. Additionally, a thinner device will have less sensitivity to external temperature changes. These benefits must be weighed against drawbacks of a thinner structure, which include lower quantum efficiencies and greater fragility.

A reduced thickness can reduce resel sizes because it reduces the space-charge induced spread in the avalanche current. This could reduce the requisite current and energy for thinner devices, depending on the effect used. For the thermooptic effect, the modulation is found to be independent of device thickness if greater than twice the junction depth. This assumes that voltage and current are kept constant. On the other hand, if the free-carrier effect is used, the needed requisite current is inversely proportional to thickness, which will automatically occur with thickness reduction if the overvoltage ΔV is kept constant and external resistance is made negligible. The breakdown voltage V_B, on the other hand, is reduced in proportion to the device thickness and is typically much larger than the overvoltage. Hence the peak power, $(V_B+\Delta V)\Delta V/R_D$, therefore decreases as the device is thinned (Refer to Eqs.(16)-(22) for notation). Furthermore, shorter electrical pulse durations are allowed with the free-carrier effect and this will further reduce the required energy per bit to much lower values in this case. Taken together, all these considerations suggest that a reduction in thickness by a factor of two for a later thermooptic device and a factor of 10 to a free-carrier-based device.

The depth of the breakdown region within the device is another parameter that might be varied to advantage for the PCSLM application. The breakdown region typically occupies only a fraction of the device thickness. If the breakdown region is thinner, then theory and experiment indicate that the radius of the electrical discharge will be smaller; thus a smaller amount of current will be required to create the same temperature change over a smaller area, thus enhancing resolution. This also gives an equivalent optical response with less heat consumption and this will ease cooling requirements, especially for the higher-throughput applications. However, reduction of the radius of the discharge by more than a factor of two will not be of much benefit, because the spot size would be so small that diffraction effects would reduce the optical response. Also. a thinner breakdown region can up the required breakdown voltage. Hence a reduction in the thickness of the breakdown region by a no more than a factor two should be considered for a future device.

7.1.4 Material Specifications

The above requirements depend on the deposition for a known current of known duration. To deposit a specified current over a specified duration requires that the electrical properties of the device be uniform in time and position. The two relevant electrical quantities are the resistivity and the breakdown voltage. The resistivity is already highly uniform for any avalanche photodiode. The steady-state current of the diode was experimentally observed to vary by less than 10 % over the surface of the 0.5 mm diode, over the desired duration, with the desired voltage bias and external resistance. This suggests that the requisite electrical uniformity is available with off-the-shelf devices. It does not prove that the needed uniformity is available because the breakdown site may move over the duration of the electrical pulse, even though the overall device current may remain nearly constant.

To estimate the needed uniformity of breakdown voltage, one requires that the probability of breakdown vary little over the face of the device. A detailed stochastic model has been developed as given in Section 3.4.1. Following the analysis there using Eq. (62) of that section, one estimates the chance of a parasitic breakdown changes by less than 20% of the BER if the breakdown voltage variations are less than 1 Volt across the face of the device.

7.1.5 Extensions for Dynamic Range

Another issue is that of device dynamic range. A device with single-photon response is inherently limited in its dynamic range of response to multiple photons. However, there is a least one trick for enhancing dynamic range. The pulse format used in the experiment entails a delay of

up to 50 nanoseconds between the writing and reading pulses. If the APD voltage is periodically pulsed within this period, then the average current over the delay will depend on the re-excitation of the device by different photons arriving at different times. It should be noted that this quenching will occur automatically if the APD is operated near breakdown. Thus if the writing pulse is spread out in time, the average current will depend on the arrival rate of photons at the device. More to the point, the thermal response will be proportional to the number of photons arriving during the write/read delay. This implies a dynamic range that is limited by the number of quenches that can be implemented within a 50 nanosecond delay; about 1 quench/reset can be achieved every 2 nanoseconds. Therefore, this approach could improve the dynamic range of the device up to about $50/2 = 25$. Of course, a key assumption is that noise-induced re-avalanching is not significant—thus this technique requires experimental verification.

7.2 HIGH-THROUGHPUT OPERATION

For high-throughput applications, multi-resel operation is important. For multi-resel operation, all the specifications for the single-resel operation apply and then some. For example, it is anticipated that current-deposition uniformity and parasitic noise will require some control above that needed for single-resel operation. Control of the electrical current level and timing, combined with transparent electrodes (or screen-type or matrix-type if cheaper) may be necessary. A somewhat higher photon-incidence rate might also be useful for re-seeding of the excited resels to reduce the effect of parasitic avalanches.

7.2.1 Current Specifications

For high-throughput applications multi-resel operation is important. The absence of pixellation would at first glance imply that different resels at different locations would receive different currents and therefore the response would be spatially variable. This variability is self-limiting, however, because localized high currents cause localized heating the results in a decrease in the local avalanche gain and an increase in the local resistivity. Thus, multi-resel operation is not immediately dismissable as impractical. To get uniformity of current deposition, evidently sufficient current must be made available to the device to accommodate the expected number of "on" resels.

A potential aid in improving uniformity of current delivery is an improved electrode design. Present electrode designs for APDs consist of ring on the front face that encircle the active region. Obviously, this geometry might provide extra current to avalanches at the edge of the active region

·in preference to those near the center. This potential problem can be solved by depositing a transparent electrode or a screen or matrix electrode on the front face of the APD. The screen would consist of a deposition of conducting wires that are about 2 microns in thickness and spaced every pixel. This screen grid would ensure that current is evenly provided and would also ensure uniform voltage across the entire breakdown region of the device, especially if a reach-through structure is used.

Device manufacturers [11,19] state that such electrodes are feasible and inexpensive. The procedure involves creating a mask and using lithography to deposit a transparent Cr/Au or indium tantalum oxide (ITO) on bare silicon on the front surface. If a screen is desired, it need only be deposited on the front face. The rear face already has a large-area electrode producible using ion implantation or annealing. This is also consistent with the suggested design, since a bare silicon front face is acceptable from optical considerations. The manufacturer is currently capable of forming masks with 3-4 micron resolution, which is acceptable but not state-of-the-art. State-of-the-art lithography will achieve screens with wire thicknesses of 1 micron.[19] The initial cost of creating, testing and improving such a mask for the present device is about $20,000 (ROM). Thereafter, the device cost will be within a factor of two of the off-the-shelf device.[12,19] Thus, the thicker reach-through structures should be available for less than 8 cents per pixel in mass production and the shallow-junction structures should cost about only about 0.01 cents per pixel using epitaxial manufacturing techniques. For larger devices, say 0.5 cm, the cost would increase roughly in proportion to the linear dimensions of the face.

A screen electrode, if necessary, will affect the coherence of the read-out light and for this reason, some subsequent spatial filtering of the read-out wave would be desirable, used in conjunction with thinner electrode wires which will diffract light over larger, more-easily filterable angles. Thinner wires imply more electrode defects and this implies increased costs from reduced yields. An application-specific tradeoff will need to be conducted if this approach is worthwhile. The transparent electrode using ITO or Cr/Au is preferable from this point of view.

7.2.3 Noise

The primary noise source is expected to be parasitic avalanching for multi-resel operation. Based on the analyses above, a straightforward fix is use of an electrode that guarantees uniform current deposition. A uniform transparent electrode may be sufficient, but passive matrix addressing will almost certainly provide the needed uniformity. Two other straightforward

conceptual solutions are available to minimize parasitic breakdown. The first involves current control. The second involves voltage control. These two alternatives are discussed in turn.

The basic equation for the bit error rate (BER) from parasitic avalanching and from all other sources is given by Eq.(28) of Section 3.4. The relevant case is one in which the current is in or near steady-state. Parasitic avalanching is the dominant noise source and in which the generation rate of a parasitic avalanche is much less than the decay rate of a single isolated minimum-current filament. Then

$$BER \approx 0.5 p_p \tag{73}$$

where

$$p_p = \exp[-(n_o-1)\gamma_o t]$$
$$\gamma_o = [I_{min}/Q_o] \exp(-r/r(\lambda)) P(V_{ss}-V_B)$$
$$\approx [5 \times 10^{-5} / 1.6 \times 10^{-10}] \times 0.1 \times 0.02 = 150 \text{ per sec} \tag{74}$$

The parameters in this equation are: n_o = the number of active resels in a neighborhood of the subject resel, multiplied by 4 to insure adequate thermooptic response; t = one-half the duration of the electrical pulse, the minimal filament current I_{min}, the photon generation rate per coulomb of carriers, Q_o, the pixel radius r, the absorption scale for the generated photon $r(\lambda)$ and the probability of avalanche $P(V_{ss}-V_B)$ at overvoltage $V_{ss}-V_B$.

Thus to reduce the bit error rate, one may easily reduce the duration of the electrical pulse, increase the spacing r between pixels or reduce the voltage between pixels. A very significant way to reduce the BER is to use multiple pulses per bit; then the error probability is just the product of (small) error probabilities per each pulse and the bit error rate goes down exponentially. This approach is detailed in the next section.

7.2.3.1 Current Control for Noise Reduction

Even with control of the current as discussed above, parasitic breakdown is still possible, especially when larger currents are supplied for many resels. This parasitic effect can be minimized by pulsing the overvoltage over the breakdown only at times when a signal is expected and the signal is accordingly compressed into relatively short time intervals, e.g., < 100 nsec, for best noise rejection. The pulsing is automatic if operation is at voltages close to the breakdown voltage because of self-quenching. This approach is similar to that suggested in Section 7.1.5 for extending the dynamic range of the device. The basic idea, as shown in Figure 22, is to force the

• available current through the desired resels. This can be accomplished by repeated re-seeding of the active resels: the optical input signal re-excites the desired pixels, but the noise avalanches do not repeat at the other pixels, on average. The amount of reseeding depends on the degree of suppression required—complete suppression should occur when the reseeding rate is about equal to the rate of generation of secondary photoemission, i.e., about one photon per 10^{10} (Ref. 7) photoelectrons, which corresponds to about 60 photons per write pulse.
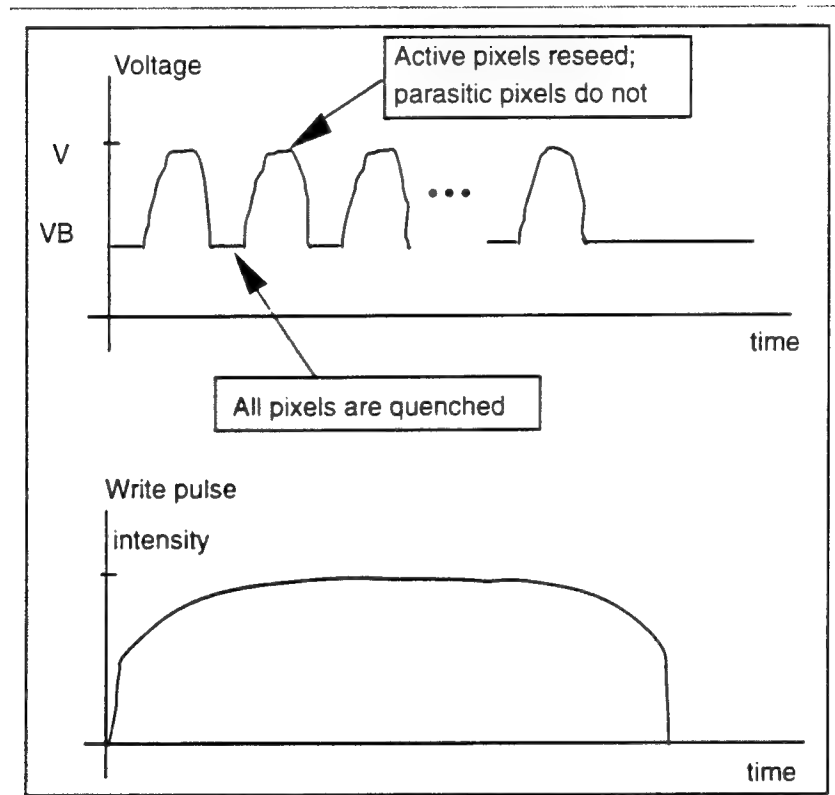
Figure 22. Temporal voltage modulation as a means for reduction of parasitic breakdown

Current control has the effect of reducing the time t in Eq.(74) above. If the reduction is about a factor of 10 from 50 nanoseconds to 5 nanoseconds, the BER is then decreased to about 0.5 {1-$(1-p_p)^{10}$} $\approx 2.5 \times 10^{-55}$ for single-resel operation and 2.6×10^{-32} for 50 active pixels in a neighborhood. This error rate is negligible compared to other noise sources. It should be noted that these BERs should be representative of large-area, very-high-throughput devices because only about 50 neighboring resels can contribute secondary photoemission to a given resel, because of the spacing of the pixels (≈ 6 microns) and because of the absorption length of secondary photoemission (< 10 microns).

When the current is modulated to reduce noise, the device may acquire dynamic range roughly in proportion to the number of modulation cycles, as discussed in Section 7.1.5. In such cases, a more appropriate noise figure of merit is the SNR. The SNR is easily calculated assuming that electrical excitation of the diode at different cycles are statistically independent and that the noise and signal excitation processes are statistically independent. Denoting the number of cycles by N and denoting the probability of excitation by signal as p_s and by noise as p_{err}. Eqs.(30)-(31) give the SNR:

$$SNR = \frac{\sqrt{N}(p_s + p_{err})}{\sqrt{p_s(1-p_s) + p_{err}(1-p_{err})}} \tag{75}$$

where, for example, $N \approx 10$. $p_s \approx 1-10^{-2}$, $p_{err} \approx 5 \times 10^{-5}$, yielding an SNR of about 31.6, which is obviously more than necessary for most applications, since it corresponds to a bit error rate that is many orders of magnitude less than the standard 10^{-12}.

If such temporal voltage/current modulation is not desirable, alternative means of improvement are available. The possibility of voltage control discussed in the next section offers equally dramatic improvements that exceeds most potential requirements.

7.2.3.2 Voltage Control for Noise Reduction

Referring to Figure 23, one may see that spatial isolation of the voltage will inhibit parasitic breakdown because reduced voltage surrounding a pixel will reduce parasitic avalanches where they are most likely to occur.

The effect of this spatial voltage modulation can be seen through Eqs. (73) and (74). The probability of breakdown drops essentially to zero in the dead zones of low voltage between pixels and the radius of the pixel, r, may be increased as well. If the pixel radius, here set by the electrode spacing, is increased to about 12 microns from 6 microns and the probability of breakdown voltage is reduced to about 0.001, then the BER for $50/2^2$ active resels in a neighborhood is estimated at about 1.8×10^{-5}, using this approach.

This result clearly suggests that secondary photoemission and associated noise are surmountable by spatial voltage modulation as well as temporal voltage modulation.
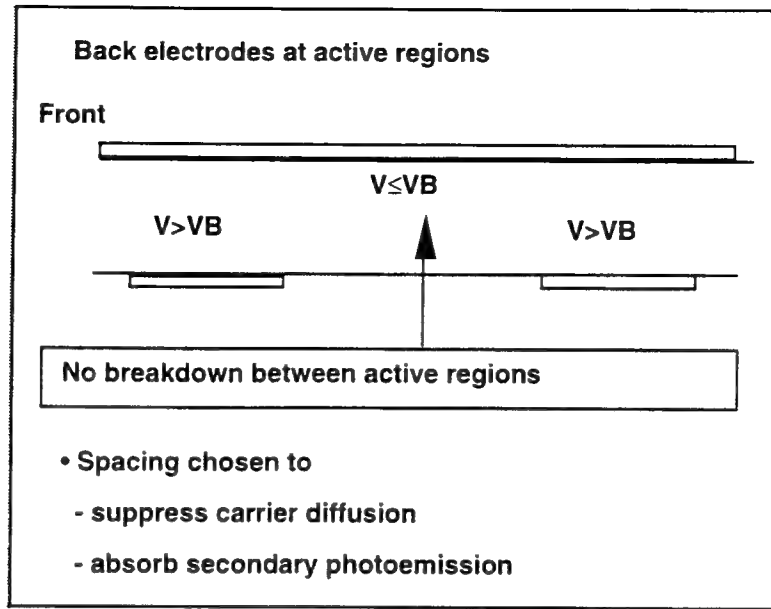
*Figure 23. Spatial voltage isolation as a means for reduction
of parasitic breakdown.*

7.2.4 Thermal Control

Thermal control is needed for single-pixel-per-frame applications and moreover for high-throughput applications. The device needs to have a uniform, constant temperature to maintain optical bias and to control the electrical properties of the device. This will occur only if heat is removed from the device at the rate at which it is added, i.e., if thermal runaway is avoided. The rate at which it is added depends on the number n of excited pixels per frame and the number of frames per second f.

$$\text{Heat added per sec} = dH/dt = P \, n \, f \, \Delta t, \tag{76}$$

where P is the peak power per pixel needed to create the optical contrast modulation response and is approximately 100 mW per active pixel; and Δt is the duration of the electrical response which is approximately 50 nanoseconds. From these parameters, the requisite electrical energy, $E = P\Delta t$, is equal to 5 nJ for the thermooptic effect with the present device. To scale to other devices, use the formula $E = c_p \Delta T A \Delta z/3$, where c_p is the specific heat per unit volume of silicon, ΔT is the peak avalanche-induced temperature difference, A is the area of heating and Δz is the diode depth (40 microns for a reach-through device and 4 for a shallow junction device). From Eq. (76), the

rate of heat production can be computed assuming a large device ($A_d = 0.25$ cm^2) and full utilization of the device area with a pixel every 6 microns ($A_p = 36$ microns^2):

$$n = (1/2) \, A_d \, / A_p \qquad (77)$$

From this one computes a <u>maximum</u> expected rate of heat production, for a fully utilized, large device, equal to

$$dH/dt = = 1.7 \times 10^{-3} \times f \text{ (40-micron reach-through device)} \qquad (78)$$

For example, if the frame rate is 1 MHz, then the heat production is 1700(!) Watts for a reach-through device. In contrast, a thermoelectric cooler can only remove about 1 mW for a 0.5 mm device and perhaps 0.1 Watts for a larger 0.5 cm device; hence from Eq. (7.6) frame rates of up to only about 590 Hz for a shallow-junction device are supported by thermoelectric technology .

How else can heat be removed from the device? A negligible amount of heat is removed by the flow of the electron-hole gas via the well-known Thomson effect. Thus the bulk of heat dissipation must occur through transfer to the surroundings. For transfer to the surroundings, the rate of heat creation must be balanced by heat dissipation rate through the front and back surfaces. The heat dissipation rate is set by the requirement that the electrically-generated energy is fully dissipated between frames. The heat dissipation rate is achieved by allowing sufficient time for the heat to dissipate through the APD structure and by maintaining a difference in temperature between the front or back surfaces of the device and the surrounding medium. Thus the thermal flux balance gives

$$\text{Heat generated per pixel per frame} = E \leq 2\kappa\Delta T \, A \, / \, (0.5\Delta z f), \qquad (79)$$

where κ is the thermal conductivity of silicon, equal to 1.48 W/cm/K. Combining this with $E = c_p\Delta T A \Delta z/3$ gives a limit on frame rate from thermal considerations:

$$f \leq 12\kappa/ \, c_p\Delta z^2 = 80 \text{ MHz (4 micron shallow-junction)}$$
$$= 800 \text{ kHz (40 micron reach-through)} \qquad (80)$$

Once the heat has diffused to the surface of the diode, it must be removed by diffusion or convection. Diffusive cooling will probably be inadequate for the highest frame rates, given the

total power dissipation estimated above. For convection cooling, the rate at which heat is removed
is

$$\text{Heat removed per sec} = (dm/dt)\, c_{pa}\, \alpha\, \Delta T \qquad (81)$$

where dm/dt is the rate of mass flow of coolant across the diode; c_{pa} is the specific heat per unit
mass of the ambient flow, which is 1007 J/kg/K for air or 4184 J/kg/K for water and $\alpha\Delta T$ is the
surface temperature of the diode relative to ambient. Now, the diode may operate well above room
temperature if the bias voltage and the optical bias are adjusted accordingly. Hence it is not
unreasonable to set $\alpha\Delta T$ to 20 C. One then finds a needed mass flow versus frame rate, again
assuming a device that is both large and fully-utilized:

$$dm/dt = dH/dt \,/\, (c_{pa}\, \alpha\, \Delta T\,) = 8.5 \times 10^{-8} \times f \;\text{(kg/sec in air)} \qquad (82)$$

From these mass flow rates, one may deduce flow velocities using the relation

$$dm/dt = \rho\, v\, A_f \qquad (83)$$

where $\rho = 1.29$ kg/m^3 is the density of air at STP and 10^3 kg/m^3 for water; and A_f is the transverse
area of the flow, at the diode. One may estimate this area to be the width of the diode, about 0.5
cm for the largest diodes envisioned, multiplied by about the same for the height of the flow
channel. One then obtains a flow velocity equal to

$$
\begin{aligned}
v &= dH/dt \,/\, (c_{pa}\, \alpha\, \Delta T\, \rho\, Af) \\
&= 2.6 \times 10^{-3} \times f \;\text{(m/sec for air, reach-through)} \\
&= 8.1 \times 10^{-7} \times f \;\text{(m/sec for water)} \qquad (84)
\end{aligned}
$$

It is seen that reasonable flow velocities with air are found at the intermediate frame rates. A flow
velocity of up to 10 m/sec might be reasonable; thus steady-state frame rates of up to 4 kHz are
expected to be practical for air cooling and frame rates up to 12 MHz with 10 m/sec of water flow,
based on thermal considerations for the thermo-optic effect in the thicker reach-through devices.
Whether a coolant system with such flow rates are economical is yet another question. Note that
any flow should be across the back surface of the diode, to avoid aberrations in the optical path that
could be caused by turbulent flow.

Thus convective cooling is needed in applications requiring frame rates in excess of 600Hz. For frame rates less than this or with less than full utilization of the diode, no convective cooling is needed, but thermoelectric temperature control is useful to avoid ambient temperature fluctuations. It is seen that convective cooling with air is achievable for steady-state frame rates of up to 4 kHz. Convective cooling with water allows 12 MHz to be achieved. The limiting information flux in such cases is 33 Terabits per second per square centimeter.

7.3 DESIGN SUMMARY

In summary, prospects for low-light-level operation are excellent. 80 MHz frame rates, 3 micron pixel radii, 7:1 contrast ratios and SNR's greater than 30 (bit error rate$<<10^{-12}$) should be achievable. Such devices are suitable for applications at low light levels, such as laser radar sensors or low-light-level imaging detectors. For a large-area, multi-resel device, additional device testing is needed and minor electrode development is needed. The device would appear as in Figure 24. Preliminary specification of such large area, high-performance devices follow for both low and high throughput. This specification is based primarily on lab results and discussions with APD manufacturers (EG&G and Rockwell Science Center-Anaheim) on existing manufacturing processes. This device is suitable for high-throughput optical processing, target identification, rapid beam steering and serial-to-parallel data conversion.

7.4 SPECIFICATIONS SUMMARY

Two options are available: a shallow-junction device made at Rockwell Science Center or a reach-through device made using existing facilities at EG&G Optoelectronics; both might appear as shown in Figure 24. The shallow-junction device is best when low cost, low energy, low voltage or higher speed are most needed, but the reach-through structure is best when high quantum efficiency is desired. A shallow-junction device is a factor of 100 cheaper than a reach-through device because of different manufacturing processes and is expected to consume a factor of 4 less energy per bit. The latter is specified first. The cheaper, faster shallow-junction device is second.
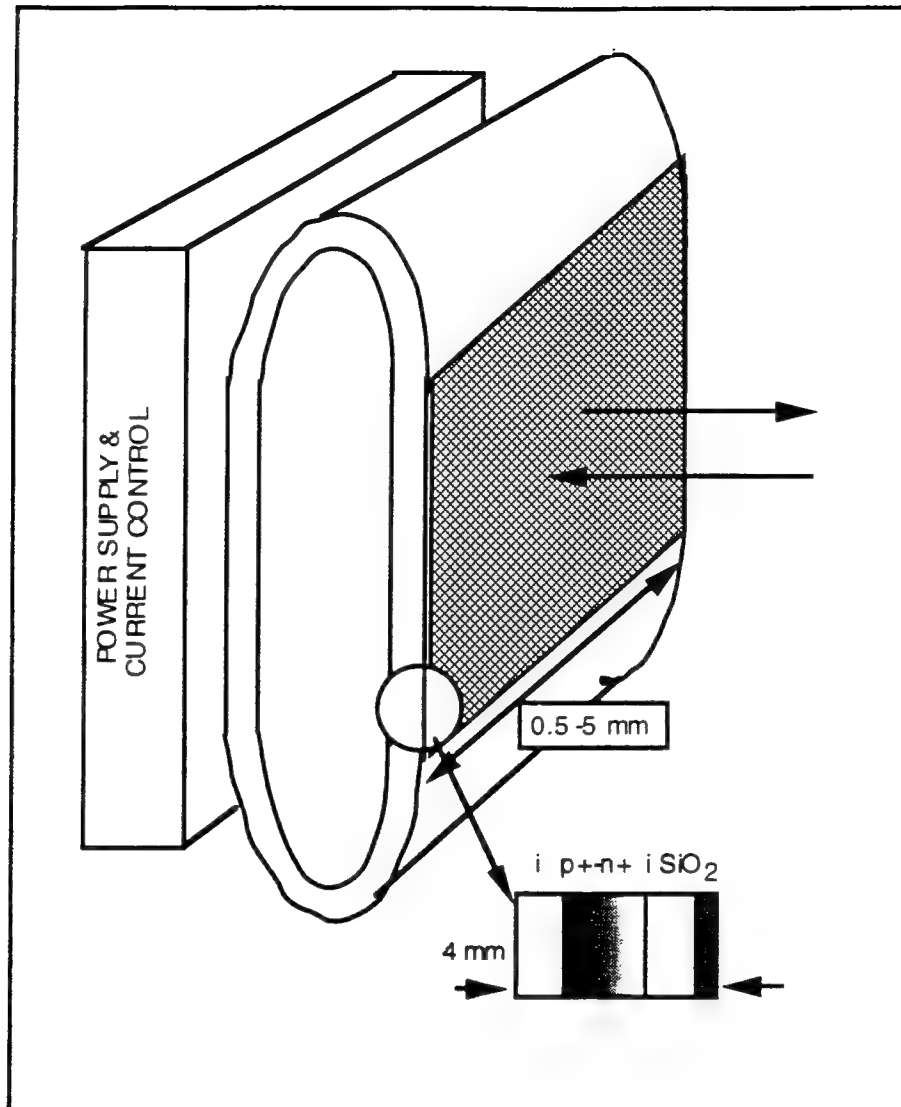
Figure 24. Schematic of a high-performance device

Table 3 Specifications for a Low-Light Device

Parameter	Value	Comments
Total device cost (80x80)	< $500	Estimate for reach-through based on EG&G prices
Total device cost(800x800)	< $2000	Rough estimate based on EG&G prices
Energy per bit	5 nanoJoules	Scaled from lab data.
Operating voltage	140 Volts	Determined from lab effort; V_B = breakdown voltage = 120 V; 20 micron thickness
Frame rate(water cooled)	< 3.2 MHz	Water-cooled, 20 micron device thickness
	< 20 KHz	Air-cooled 20 micron device

Table 3. Specifications for a Low-Light Device (continued)

Parameter	Value	Comments
Throughput	2.0 Tbits/sec	Water-cooled
....	128 Gbits/sec	Air-cooled; limit set by thermal dissipation.
Number active resels	<800 x 800	Based on largest device that can be made with tolerable noise
Resel radius	3.0 microns	Based on lab data
Dynamic range	10	Ratio of max pulse bias duration to min pulse bias cycle; also Δ temperature
Write pulse energy	5-300 photons	Per resel; based on lab data, high value used in conjunction with cyclic pulse biasing for increased dynamic range, reduced noise
Write pulse energy	5-300 photons	Per resel; based on lab data, high value used in conjunction with cyclic pulse biasing for increased dynamic range, reduced noise
Bit error rate	< 10-13	Based on lab and published data. See sections 3.4 and 7.2.3.1.
Contrast ratio	70 % max	Based on temp. tuning of optical bias.
Write λ	600-1060 nm	Based on quantum efficiency of APD.
Read λ	1060-1500 nm	Based on lab data, low absorptions and optical resolution criteria.
Optical losses -read beam	91 % (on)	For 7:1 contrast device.
	97 % (off)	" "
	23 % (on)	For 2:1 contrast device
	12 % (off)	" "
Device width	< 0.5 cm	Based on manufacturer noise specs.
	< 120 microns	For near-term, based on optical thickness tolerance and manufacture process control for reach-throughs
Device structure	reach-through	Based on lab data and analysis
Device thickness	20 microns	Reduces external voltages to 140V
Load resistance	2-50 kΩ	Based on lab effort, gives enough response, yet avoids parasitic avalanches.
Pulse bias duration	50 nsec	Time during which voltage is biased above breakdown; based on lab results

Table 3. Specifications for a Low-Light Device (continued)

Parameter	Value	Comments
Duty factor	0.3 - 6 %	Product of pulse bias duration and frame rate
Pulse bias cycle	5 nsec	Reset time for greater dynamic range; based on max electrical switching rates; also reduces parasitics
Temperature tuning	20 Kelvin	Based on needed optical bias Assume 10 % yield is acceptable from existing manufacturing processes.
Temperature tolerance	1 Kelvin	Required to maintain proper optical bias
Temperature control	thermoelectric	For frame rates < 600 Hz or 1MHz at low light levels
	convective w air	For 600Hz- 20 KHz device; 10 m/sec flow at back surface.
....	convective w water	2.5 m/sec flow for 3.2 MHz
Write pulse duration	1-50 nsec	Based on needed duration of electrical excitation.
Read pulse duration	< 30 nsec	Based on duration of best response.
Read/Write Delay	< 50 nsec	Based on lab data.
Total device lifetime	$\gg 10^4$ frames	Based on lab results
	....	.....
Electrode type - back	Standard chrome-gold	....
Electrode type - front	Standard ring	For single-pixel-per-frame device
....	Transparent Cr/Au	For multi-resel operation.
....	Screen or matrix	May need for improved uniformity, noise suppression
Electrical Uniformity	1 V	Not a design issue based on lab data and manuf. specs.
Optical Uniformity	5 nm	< 10 % contrast modulation variation across device face.

Table 4. Specifications for a high-speed array device
(Values shown only where different from above)

Parameter	Value	Comments
Total device cost	$2	Rough estimate for 80x80
	$65	Rough estimate for 800x800 based on Rockwell Science Center estimate for custom epi
Physical effect	free-carrier	permits reduced energy per bit and increased speed
Energy per bit	1.2 nJ	Scaled from lab data to reduced thickness, pixel size
Voltage	45 Volts	Scaled from lab effort; V_B = breakdown voltage= 25 V
Device structure	shallow junction	Based on lab data and analysis
Device thickness	4 microns	Reduces external voltage to 45 V
Resel radius	2.0 microns	Based on lab data.
Device size	0.5 cm	Achievable and meets thickness tolerances using epitaxial fabrication.
Number active resels	< 800 x 800	Based on largest device that can be made with tolerable noise.
Bit error rate	< 10^{-10}	Achieved with thinner structure, shorter write pulses, more photons, no cyclic biasing in 1 nsec.
Contrast ratio	40 %	Free-carrier effect is weaker.
Dynamic range	1	No cyclic biasing in 1 nsec
Frame rate	< 48 MHz	Based on thermal dissipation with water, reduced energy/bit.
Max throughput	< 31 Tbits/sec	Product of max frame rate and max resels per frame; consistent with backside water cooling.
Pulse bias duration	1 nsec	Time during which voltage is biased above breakdown; based on lab results
Duty factor	1.2 %	Product of pulse bias duration and frame rate
Write pulse duration	<1.0 nsec	Based on needed duration of electrical excitation, device speed.
Read pulse duration	< 30 nsec	Based on duration of best response.
Read/Write Delay	< 1 nsec	Based on lab data.
Write pulse energy	5-50 photons	Per resel; based on lab data, high value used for reduced bit error rate

Table 4. Specifications for a high-speed array device
(Values shown only where different from above)

Parameter	Value	Comments
Temperature control	convective w water	For high-throughput device;10 m/sec flow at back surface.
Temperature control	± 1 C	thinner device, reduced sensitivity; but less contrast modulation too
Electrode type -back	Standard chrome-gold	
Electrode type-front:	Transparent Cr/Au or	Needed for improved
	Screen or matrix	uniformity, noise supression

8.0 REFERENCES

1. S. M. Sze, *Physics of Semiconductor Devices* (Wiley, New York. 1985).

2. R. Kuvas and C. A. Lee, "Quasistatic Approximation for Semiconductor Avalanches," J. Appl. Phys., **41** (4), pp. 1743-1755 (1970).

3. R. H. Haitz, "Model for the Electrical Behavior of a Microplasma," J. Appl. Phys., **35**, pp. 1370-1376 (1964).

4. T. E. Ingerson, R. J. Kearney and R. L. Coulter, "Photon-counting with photodiodes," Appl. Opt., **22**, pp. 2013-2018 (1983).

5. A. Lacaita, S. Cova, A. Spinelli, F. Zappa, "Photon-assisted avalanche spreading in reach-through photodiodes," Appl. Phys. Lett., **62** (6), pp. 606-608 (1993). See also A. Lacaita, M. Mastrapasqua, M. Ghioni and S. Vanoli, "Observation of avalanche propagation by multiplication in p-n junctions," Appl. , Phys. Lett., **57** (5), pp. 489-491 (1990).

6. S. M. Horbatuck, D. F. Prelewitz and T. G. Brown, "Avalanche enhancement of optical nonlinearities in semiconductor junctions," Appl. Phys. Lett., **56** (24), pp. 2387 - 2389 (1990).

7. J. H. Swoger, S.J. Kovacic, "Enhanced luminescence due to impact ionization in photodiodes," J. Appl. Phys., **74** (4), pp. 2565-2571 (1993).

8. R.A. Soref and B.R. Bennett, "Electro-optical effects in silicon," IEEE J. Quantum Electron., **QE-23**, pp. 123-129 (1987).

9. G. Cocorullo, M. Iodice and I. Rendina, "All-silicon Fabry-Perot modulator based on the thermo-optic effect," Opt. Lett., **19**, pp.420-422 (1994).

10. Y.M. Liu, X. Xiao, P. R. Prucnal and J.C. Sturm, "All-optical switching in an asymmetric silicon Fabry-Perot etalon based on the free-carrier plasma effect," Appl. Opt. **33**, pp. 3871-3874 (1994).

11. Private conversation, R. Seymour and A. MacGregor, EG&G Canada, Vaudreuil, Canada. (514)424-3300.

12. RCA Electro-Optics Data Sheet, part C30902S, "High-Speed Solid-State Detector for Fiber-Optic and Very-Low-Light-Level Applications," (EG&G, Vaudreuil, Canada),and private communications.

13. M. Born and E. Wolf, *Principles of Optics*, pp.110-117 (Pergamon, Oxford, 1980).

14. R. Holmes, R. Myers and C.Duzy, "A linearized theory of transient laser heating in fluids," Phys. Rev. A, **44**, pp. 6862-6876 (1991).

15. N. A. Nazarova, G.I. Romanova and A. D. Yas'kov, "Refractometric characteristics of silicon," Sov. J. Opt. Technol., **55** (4), pp. 220-224 (1988).

16. J. Pankove, "Optical Processes in Semiconductors," pp. 89, 229, 230, 379 (Dover New York, 1975) and references therein.

17. D. Jager, J. Opt. Soc. Am. B. **6**, pp.588 (1989).

18. N. G. Woodward, E. G. Hufstedler, G. P. Lafyatis, "Photon counting using a large are avalanche cooled to 100 K," Appl. Phys. Lett., **64**, pp.1177-1179 (March 1994).

19. Private conversation, J. E. Huffman, Rockwell Science Center, Anaheim, CA. (714)762-8111.

20. R. K. Jain and M. B. Klein, "Dengenerate Four-Wave Mixing in Semiconductors," in *Optical Phase Conjugation*, R.A. Fischer, ed., pp. 307-415 (1983).

21. S. Y. Auyang and P. A. Wolff. "Free-carrier induced third-order nonlinearities in semiconductors," J. Opt. Soc. Am. B, **6**, pp. 595-605 (1989).

22. R. A. Soref, "Silicon-Based Optoelectronics," Proc. IEEE, **81**, pp.1687-1706 (1993).

23. J. S. Heeks, "Some Properties of the Moving High-Field Domain in Gunn Effect Devices," IEEE Trans. on Electron Devices, **ED-13**, pp. 68-79 (1966).

24. S. R. Bowman, W. S. Rabinovich, C. S. Kyono, D. S. Katzer and K. Ikossi-Anastasiou, "High-resolution spatial light modulators using GaAs/AlGaAs multiple-quantum wells," Appl. Phys. Letters, **65**, pp.956-958 (1994).

25. ARPA/MTO Optoelectronics Program Review, June 13-17, 1994, Monterey, CA. Talks by OETC, Honeywell, Stanford University.

26. *Handbook of Optical Constants of Solids*, E.D. Palik, ed. (Academic Press, 1985).

APPENDIX A. RELATED PUBLICATIONS AND PATENT ACTIVITY

The following is a list of publications and patent disclosures related to the subject contract.

PUBLICATIONS:

J. Hunt and R. Holmes, "Observation of Optical Response of Avalanche Photodiodes at Photon-Counting Light Levels," Appl. Phys. Lett., **64**. pp.2925-2927 (1994).

J. Hunt and R. Holmes, " Thermo-Optic Investigation during Electrical Breakdown in Avalanche Photodiodes," J. Appl. Phys. (Nov. 1, 1994).

J. Hunt and R. Holmes, "Spatial Light Modulation of Avalanche Photodiodes at Photon-Counting Light Levels," Paper CTuD5, CLEO 1994.

PATENT DISCLOSURES

Rocketdyne Disclosure 91R101—Photon Counting Spatial Light Modulator with APD Structure

Rocketdyne Disclosure 94R013—Non-Destructive Optical Method for Characterization of Semiconductor Structures

Rocketdyne Disclosure 94R053—Means for Reduction of Parasitic Avalanching for Improved SLM in APD Structures

Rocketdyne Disclosure 94R052—Optically-Addressed Display Device using APD Structures

Rocketdyne Disclosure 94R057—Multi-Color Read-out of an Optically-Addressed Flat-Panel Display Device.

Rocketdyne Disclosure 94R043—Circuit for Biasing Avalanche Photodiodes in Active-Quench Mode for Spatial Light Modulation